The spreading of facultative H3K9me3-heterochromatin drives congenital disease

Chen Wang[1,2,#], Wei Zhang[1,#], Xue-Lin Chen[1,#], Wen-Fei Wang[1,#], Yong-Hao Li[2,#], Jian-Feng Chang[1,2,#], Xiao-Bo Guo[1], Yuan-Ya Jing[1], Ya-Bin Li[1], Xin-Yi Lu[3], Yu-Tong Li[3], Kai Liu[1], Jian-Quan Ni[2,3,*] and Fang-Lin Sun[1,2,4,*]

[1]School of Life Sciences and Technology, Tongji University; Shanghai 200092, China

[2]Tsingtao Institute for Advanced Research, Tongji University; Tsingtao 266073, China

[3]School of Medicine, Tsinghua University; Beijing 100084, China

[4]Alpha Institute of Natural Medicine, Tongji University; Shanghai, 200070, China.

[#]These authors contributed equally to this work.

*Corresponding author.

Email: sfl@tongji.edu.cn; nijq@mail.tsinghua.edu.cn

Abstract

Heterochromatin marked by trimethylated histone 3 at lysine 9 (H3K9me3) plays fundamental roles in reprogramming to direct cell fate determination in higher eukaryotes. However, the upstream factors that guide the establishment and spreading of H3K9me3-heterochromatin, leading to human developmental malformations, remain elusive. In this study, we found that Cdk13, a member of RNA polymerase II (RNAPII) kinase, suppresses congenital heart syndrome by preventing global facultative H3K9me3-heterochromatin spreading. Additionally, Cdk13 directs the phosphorylation of a large set of heterochromatin proteins at specific sites, which are required for the interaction between HP1 and histone H3K9 methyltransferases. Furthermore, we identified a compound, an inhibitor of heterochromatin regulators, that can alleviate syndromic heart defects in *Cdk*13-mutant mice through the inhibition of H3K9me3-heterochromatin spreading. In summary, this study reveals a novel role and mechanism of Cdk13-triggered facultative H3K9me3-heterochromatin spreading in human genetic disease and paves the way for the treatment of congenital heart syndrome.

33

34 Facultative heterochromatin, marked by trimethylated histone 3 lysine 9 (H3K9me3), plays
35 essential roles in cell lineage specification and maintenance of cell identity by silencing
36 undesired genes (Jenuwein and Allis 2001; Grewal and Jia 2007; Riddle and Elgin 2018; Moazed
37 2011; Allshire and Madhani 2018; Nicetto and Zaret 2019). The writers and readers of canonical
38 heterochromatin are key factors in initiating the assembly and spreading of H3K9me3-
39 heterochromatin. The histone methyltransferases Su(var)3-9/Suv39h1/Clr4 'write' H3K9me3, and
40 the heterochromatin protein HP1 serves as a 'reader' of H3K9me2/3 (Hall et al. 2002; Volpe et al.
41 2002; Becker et al. 2017; Nicetto et al. 2019). Additionally, nuclear RNAs, meiotic messenger
42 RNA elimination, and RNA interference machinery are all critical regulators of H3K9me3-
43 heterochromatin (Zofall et al. 2012; Hiriart et al. 2012; Lee et al. 2013; Yamanaka et al. 2013;
44 Tashiro et al. 2013; Chalamcharla et al. 2015). The mechanism that guides the dynamics of
45 facultative H3K9me3-heterochromatin spreading within gene-rich euchromatic regions, however,
46 is still largely unknown.

47 In a previous screen aimed at identifying upstream regulators of heterochromatin formation and
48 spreading (Pan et al. 2015), we discovered that dCdk12, a known kinase member that
49 phosphorylates the C-terminal repeat domain of RNAPII (Even et al. 2006; Chen et al. 2007;
50 Bartkowiak et al. 2010; Wu et al. 2018) controls the spreading of HP1 and H3K9me3 in the
51 euchromatic domains of the *Drosophila melanogaster* genome. Cdk13 in mammals is one of the
52 orthologues of dCdk12 (Dai et al. 2012; Bösken et al. 2014; Liang et al. 2015; Greifenberg et al.
53 2016). Mutations in *CDK*13 have been linked to syndromic congenital heart defects (Sifrim et al.
54 2016; Deciphering Developmental Disorders Study 2017) and other phenotypes, such as growth
55 retardation, craniofacial abnormality and intellectual disorder in humans (Bostwick et al. 2017;

56 Akker et al. 2017; Hamilton et al. 2019); however, the underlying mechanism of *CDK*13
57 mutation-resulted human genetic diseases remain elusive.

58

59 **Expansion of H3K9me3-marked heterochromatin after *Cdk*13 depletion**

60 To investigate whether Cdk13 affects H3K9me3-heterochromatin formation and cellular
61 programming in mammals, we first depleted *Cdk*13 from mouse embryonic fibroblasts (MEFs)
62 by specific short hairpin RNA (shRNA) knockdown (KD) (Supplementary Fig. 1A). *Cdk*13 KD
63 resulted in approximately a 50% reduction in the number of cells compared to the control cells
64 after 3-5 days of culture, indicating that the proliferation of MEFs requires Cdk13
65 (Supplementary Fig. 1B). Interestingly, immunofluorescence staining experiments showed that
66 the intensity of classical heterochromatin markers, such as H3K9me3, HP1α, HP1β, and
67 Trim28/Kap1, was significantly elevated in *Cdk*13 KD MEFs compared with controls (Fig. 1A,
68 Supplementary Fig. 1C,D). Markers of active chromatin, including H3K9ac, H3K27ac, and
69 H4K16ac, were significantly reduced Supplementary Fig. 1E-G). The expansion of
70 heterochromatinization upon *Cdk*13 KD was further confirmed by transmission electron
71 microscopy (TEM), and a robust increase in darker or condensed heterochromatin was evident
72 after *Cdk*13 depletion (Fig. 1b, Supplementary Fig. 2A). These findings support the notion that
73 Cdk13 in mice, similar to its orthologue dCdk12 in fruit flies (Pan et al. 2015), plays a critical
74 role in preventing the spreading of heterochromatin.

75 To examine the precise genomic distribution of H3K9me3-heterochromatin upon depletion of
76 *Cdk*13, we performed chromatin immunoprecipitation (ChIP) analysis using control and *Cdk*13-
77 KD MEFs. Following ChIP sequencing, an increased association with H3K9me3 was observed
78 in more than 18,500 known mouse genes, accounting for nearly 75.9% of known genes in the

79 entire mouse genome (Fig. 1C). This indicates a general role of Cdk13 in global heterochromatin
80 spreading at euchromatic regions. The most prominent increase in H3K9me3 peaks includes
81 gene promoters, gene exons/introns, and distal intergenic regions (Fig. 1D), corresponding to
82 18.4%, 20.5%, and 28.8% of overall increased peaks in *Cdk*13 KD MEFs, respectively
83 (Supplementary Fig. 2B). Further analysis of the increased H3K9me3 peaks distributed in the
84 promoters, untranslated regions, and exons of target genes revealed more than 10-fold increase in
85 H3K9me3 peaks compared to those in MEF control cells, calculated by the relative percentage of
86 H3K9me3 peaks (Supplementary Fig. 2B,C). In contrast, no significant change was observed in
87 the overall percentage of peaks in intronic regions upon *Cdk*13 KD (Supplementary Fig. 2B).
88 Notably, the increase in H3K9me3 in the H3K9me3-enriched genes preferentially occurred at the
89 region flanking the transcription start site (TSS) (Fig. 1E,F). While a subset of genes showed a
90 similar increase in enrichments at both the TSS and gene body regions (Fig. 1F and
91 Supplementary Fig. 2C).

92 The distal intergenic region remained to be the top H3K9me3-enriched region upon *Cdk*13 KD
93 (Fig. 1D), however, exhibited a more than 50% relative reduction in percentage of H3K9me3
94 peaks, decreasing from 60.7% in control MEFs to 28.8% in *Cdk*13 KD MEFs (Supplementary
95 Fig. 2B). The increased H3K9me3 in several euchromatic genes was confirmed by quantitative
96 PCR using anti-H3K9me3 CHIP DNA of control and *Cdk*13 KD MEF cells (Fig. 1G). Overall,
97 these results confirmed the general role of Cdk13 in preventing global H3K9me3-
98 heterochromatin spreading at euchromatic loci, containing protein-coding genes with pleiotropic
99 cellular functions including cardiomyocyte function, transcription regulation, and cell cycle
100 regulation in the mouse genome (Supplementary Fig. 2D-G).

101

102 ***Cdk*13 mutant mice display heart defects, increased heterochromatinization and specific**
103 **gene silencing in cardiomyocytes**

104 To verify the role of Cdk13 in H3K9me3-heterochromatin observed in *in vitro* cellular
105 experiments, we generated *Cdk*13-knockout (*Cdk*13$^{-/-}$) mice (Supplementary Fig.3A,B). Most
106 *Cdk*13$^{-/-}$ mice died before E14 (Supplementary Table 1), supporting a critical role of Cdk13 in
107 embryonic development. The ratio of surviving *Cdk*13$^{-/-}$ embryos at E11.5 was only 16.9% of
108 total progeny, which was much less than the expected 25%. By E13.5, the number of surviving
109 *Cdk*13$^{-/-}$ embryos dramatically decreased to 4.9% of the total progeny (Supplementary Table 1).
110 Detailed analysis of the *Cdk*13$^{-/-}$ embryos showed growth retardation as early as E9.5 and E11.5
111 (Supplementary Fig. 3C,D). Severe abnormalities were apparent in E13.5 *Cdk*13$^{-/-}$ embryos,
112 including craniofacial defects, digital anomalies, pleural/back effusion, and smaller body size
113 (Supplementary Table 2, Supplementary Fig. 3E,F), which is consistent with a previous
114 phenotypic report (Monika et al. 2019). Further dissection results showed that nearly 90%
115 Cdk13$^{-/-}$ mutant embryos displayed defective interventricular septum (Fig. 2A) and reduced
116 thickness of the ventricular walls (Supplementary Fig. 4A, B).

117 To examine the transcriptional role of Cdk13, we performed RNA-sequencing experiments.
118 RNA-sequencing analysis of gene expression in surviving E10.5 *Cdk*13$^{-/-}$ mouse hearts revealed
119 that the transcription of over 70% of affected genes was downregulated in *Cdk*13$^{-/-}$ hearts
120 compared to controls (Fig. 2B, Supplementary Fig. 4C). The reduction in transcription was
121 confirmed by qRT-PCR (Fig. 2C). Gene ontology (GO) analysis showed altered expression of
122 genes involved in homeostasis of number of cells, RNA polymerase II transcriptional factor
123 binding, and cardiac muscle cell differentiation/contraction (Supplementary Fig. 4D,E).
124 Furthermore, a comparison study revealed that two-thirds of the downregulated genes in E10.5
125 hearts overlapped with an increase in H3K9me3 of the corresponding genes in *Cdk13* KD MEFs

126 (Supplementary Fig. 4F). Immunofluorescence analysis showed a significant increase in known
127 heterochromatin markers, such as H3K9me3, HP1β, HP1γ, and Trim28/KAP-1, in E13.5 *Cdk*13^{-}
128 $^{/-}$ embryonic hearts compared to control hearts (Fig. 2D-H). Similarly, changes in
129 heterochromatin markers were observed in E10.5 *Cdk*13$^{-/-}$ hearts (Supplementary Fig. 5A-D). In
130 contrast, there was a decrease in phosphorylated RNA polymerase II at Ser2 and Ser5 was
131 evident at E10.5, E11.5, and E13.5 hearts (Supplementary Fig. 6A-F). Additionally, we
132 examined whether *Cdk*13$^{-/-}$ embryonic heart defects were linked to changes in cell proliferation.
133 The results showed a significant reduction in Ki67-positive cells in E9.5 *Cdk*13$^{-/-}$ hearts
134 (Supplementary Fig. 6G, H), compared to controls. Furthermore, the total number of cells in the
135 E13.5 *Cdk*13$^{-/-}$ mutant embryos was decreased by almost 50% (Supplementary Fig. 6I). These
136 results support the critical role of Cdk13 in development and confirm Cdk13's role in preventing
137 heterochromatin expansion and specific gene repression *in vivo.*
138

139 **Phosphoproteomic analysis of the proteins caused by *Cdk*13 knockdown**

140 To investigate how Cdk13 regulates the spreading of H3K9me3-heterochromatin, we
141 hypothesized that Cdk13 may phosphorylate heterochromatin regulators, which in turn alters
142 their interactions and subsequent heterochromatin spreading. We conducted phosphoproteomic
143 analysis on *Cdk*13-KD MEFs and control MEFs (Fig. 3A). Data from replicates of cells
144 transfected with *Cdk*13 shRNA showed 1673 downregulated phosphorylation sites within 976
145 proteins (Fig. 3B). Among the proteins with reduced phosphorylation, 69% are nuclear proteins,
146 15% are cytoplasmic proteins, and 3% are both nuclear and cytoplasmic proteins (Fig. 3C). Over
147 620 proteins carry one downregulated phosphorylation site, while the remaining proteins possess
148 two or more downregulated sites (Fig. 3D), with highly conserved motif. The top three most
149 matched preferential motifs, $_{xx}$_S_P$_{xx}$, $_{xx}$R$_{xx}$_S_$_{xx}$ and $_{xx}$_S_$_{x}$E$_{xx}$, enriched from 1639 unique

150 peptide sequence centered by downregulated phosphorylation site and extended 6 amino acid up-
151 and downstream (Fig.3E). Compared with control, the changes in the phosphorylation of specific
152 proteins in overexpression or depletion of *Cdk*13 were confirmed by Western blot
153 (Supplementary Fig. 7B). The results support the significant role of Cdk13 in phosphorylation
154 regulation, with a preference for targeting nuclear proteins.

155 The top proteins found to have altered phosphorylation are involved in messenger RNA
156 processing/splicing, and histone modifications (Fig. 3F). Specifically, more than 60 proteins
157 possess transcription coregulation activity: 26 are RNAPII-specific DNA binding transcription
158 factors, 14 are related to basal RNAPII transcription machinery binding, 9 are RNAPII
159 holoenzymes, and 11 are related to RNAPII core enzyme binding (Fig. 3F,G). Many regulators
160 of histone binding, histone methylation/demethylation or acetylation/deacetylation and gene
161 silencing were identified (Supplementary Fig. 7A).

162 Furthermore, more than 20 of the identified proteins with downregulated phosphorylation are
163 associated with heterochromatin assembly and H3K9 methylation or demethylation (Fig. 4A,
164 Supplementary Fig.7A). For instance, Setdb1, an HMT that catalyses H3K9me3, and two
165 regulators of Setdb1, Resf1 and ATFiP (Fig. 4A, B), were identified among the proteins with
166 downregulated phosphorylation sites. Therefore, Cdk13 likely prevents heterochromatin
167 spreading via phosphorylation on H3K9 HMTs. Moreover, the loss of phosphorylation at two
168 specific sites of the heterochromatin protein HP1β, S89 and S91, was observed (Fig. 4B). Both
169 sites are located within the Hinge region of HP1β, which is known to possess DNA/RNA
170 binding activity. These results therefore support the notion that heterochromatin remodelers are
171 targets of Cdk13, which may in turn contribute to the dynamics of heterochromatin spreading.
172 Overall, the phosphoproteomic analysis shows that Cdk13 is a key regulator of proteins related

173 to RNAPII transcription, most interestingly, Cdk13 was found to regulate the phosphorylation of
174 drivers involved in heterochromatin formation.

175

176 **Phosphorylation of HP1 attenuates the interaction between the master regulators of**
177 **heterochromatin**

178 To evaluated whether the affected phosphorylation of nuclear proteins participated in *Cdk*13
179 depletion-induced heterochromatinization and target gene suppression, we chose the
180 heterochromatin protein HP1 for the study. HP1 recognizes H3K9me2/3 and can also serve as a
181 critical 'hub' to recruit other heterochromatin modifiers and orchestrate the formation of
182 heterochromatin (Gerwal and Jia 2007; Eissenberg and Elgin 2014). Firstly, we conducted
183 immunoprecipitation experiments to examine the interaction between heterochromatin proteins
184 such as HP1 orthologues, and the H3K9me2/3 HMTs Suv39h2, G9a, and Setdb1 after *Cdk*13 KD.
185 Protein immunoprecipitation was performed using an antibody against HP1 orthologue and
186 nuclear extracts from control and *Cdk*13-KD MEFs. The results indicated a significant increase
187 in the affinity between HP1α and HP1β as well as H3K9me HMTs after *Cdk*13 depletion (Fig.
188 4C), supporting phosphorylation by Cdk13 prevents the heterodimerization.

189 We then examined whether the phosphorylation of specific sites on HP1, detected in the
190 phosphoproteomic analysis, played a role in the interaction with H3K9me HMTs. To mimic
191 phosphorylation loss or constitutive phosphorylation, we generated specific point mutations at
192 S89 and S91 in HP1β (Fig. 4B,D), and green fluorescent protein (GFP) tags were fused to the C-
193 terminus of wild-type HP1β and each mutant HP1β (Fig. 4D). Using the same
194 immunoprecipitation analysis approach as described above, the results showed that the HP1β
195 mutation carrying either 89/91D or 89/91E reduced the interaction between HP1β and the HMTs

196 Suv39h2, Setdb1 and G9a (Fig. 4D). This suggests that constitutively phosphorylated HP1β loses
197 its capability as a "hub" in orchestrating heterochromatin protein complexes, while the 89/91A
198 mutation, mimicking the loss of phosphorylation, increases the interaction between HP1β and
199 HMTs (Fig. 4D), which eventually promotes heterochromatin spreading. To support our
200 hypothesis, we performed IP experiments using MEFs co-transfected with Flag-tagged Cdk13
201 and the HP1β mutant plasmid. The IP results showed an interaction occurring between the
202 wildtype of Cdk13 and HP1β. However, the interaction between phosphorylated HP1β, as
203 mimicked by mutation at S89 and S91 - HP1β-89/91EGFP, and Cdk13, was dramatically
204 reduced (Fig. 4E).

205

206 **Inhibiting H3K9me3 prevents the expansion of heterochromatin and transcriptional gene**
207 **silencing triggered by *Cdk*13 depletion**

208 If the spreading of H3K9me3-heterochromatin was the cause of the observed defects in the
209 *Cdk*13 mutant embryos, we hypothesized that reducing the level of H3K9me3 could potentially
210 reverse the *Cdk*13 KD-induced HP1β association with chromatin and heterochromatin spreading.
211 This could lead to the recovery of normal transcription levels and potentially relieve the
212 developmental defects caused by the loss of *Cdk*13. Therefore, we conducted a pilot screen to
213 identify an inhibitor of H3K9me3-marked heterochromatin spreading in the *Cdk*13 depletion
214 background. From the chemical compound library, we selected fifteen inhibitors that target
215 various activities, including histone H3K9me HMTs, repressors of active H3K4 methylation -
216 LSD1, and HDAC inhibitors. After screening, we identified four inhibitors that significantly
217 reduced H3K9me3 and increased the acetylation of H3K9ac (Fig. 5A, B; Supplementary Fig.8A,
218 B). Among the four inhibitors, Givinostat (García-Rodríguez et al. 2020) (GIVI) is a pan-HDAC

219 inhibitor of HDAC1 and HDAC3, while the other two are LSD1 inhibitors, and the remaining
220 one is a G9a inhibitor (Supplementary Table 3). These findings are not surprising, as G9a is a
221 known H3K9me2/3 HMT (Shinkai et al. 2011), and HDACs, along with LSD1, are components
222 of repressive protein complexes (Shi et al. 2005) contributing to the crosstalk between histone
223 modifications (Fischle et al. 2003; Ji et al. 2019). To further investigate these interactions, we
224 conducted additional IP experiment and confirmed that HDAC3 interacts with HP1β complexes
225 (Supplementary Fig. 8C), and the phosphorylation of HP1β blocked the interaction.

226 The histone deacetylase inhibitor GIVI significantly inhibited *Cdk*13 KD-triggered H3K9me3
227 spreading, which also reduced the association of HP1β on chromatin (Fig. 5C-E, Supplementary
228 Fig.8A) and elevated the active chromatin marker H3K4me3 (Supplementary Fig.9A,B). It is
229 notable that the concentration of GIVI used, at 2.5nM, was 800-fold lower than that of LSD1
230 inhibitors and 400-fold lower than that of G9a inhibitors (Supplementary Table 3), yet it
231 efficiently prevented H3K9me3-heterochromatin and recovered H3K9ac. Further RNA
232 sequencing analysis showed that the inhibitor GIVI significantly recovered the transcription of
233 approximately 42% of genes (612 in 1471) downregulated by *Cdk*13 depletion alone (Fig. 4F,
234 Supplementary Fig. 9C). Most interestingly, among the rescued genes (Supplementary Fig. 9C),
235 numerous targets were implicated in heart, cartilage and craniofacial development (Fig. 4G,H,
236 Supplementary Fig. 9D).

237

238 **The parameters of heart defects caused by *Cdk*13 deletion are rescued by GIVI in mice**

239 To investigate whether the reduction in H3K9me3 triggered by GIVI can affect the phenotype
240 caused by the loss of *Cdk*13, we generated mice with heart-specific deletion of *Cdk*13 by
241 crossing *Cdk*13$^{fl/fl}$ mice with myosin-heavy chain 6 (*mhc*)-cre mice to obtain *Mhc-cre;Cdk*13$^{fl/fl}$

242 mice. Unlike *Cdk*13$^{-/-}$ mice, which normally died around E14 with atrial defects (Fig. 2A), the
243 *Mhc-cre;Cdk*13$^{fl/fl}$ mice were viable after birth, whereas lethality started to be observed at 159
244 days after birth, and all of these mice died before 260 days of postnatal life. In comparison, the
245 median longevity of *Mhc-cre* control mice was 329 days under the same animal feeding
246 conditions. Histological analysis was carried out to examine whether lethality was caused by
247 postnatal heart defects. Indeed, the results showed a thin atrioventricular wall, heart enlargement
248 and atrial congestion caused by dilation of the ventricles and atria (Fig. 6A), and a fourfold
249 increase in myocardial fibrosis in the *Mhc-cre;Cdk*13$^{fl/fl}$ mice at 8 months of age compared with
250 controls (Supplementary Fig. 10A). At this stage, the *Mhc-cre;Cdk*13$^{fl/fl}$ mice also showed
251 significantly decreased left ventricular posterior wall (LVPW) thicknesses at diastole (d) and
252 systole (s), increased left ventricular internal dimensions (LVID) at diastole (d) and systole (s)
253 (Supplementary Fig. 10B, upper panel), and an enlarged left ventricular volume (Supplementary
254 Fig. 10B, lower panel). In addition, left ventricular global systolic function was significantly
255 reduced, as demonstrated by the reduced left ventricular ejection fraction (EF) and left
256 ventricular fractional shortening (FS) (Supplementary Fig. 10B, lower panel), supporting the
257 requirement of Cdk13 in the heart structure and function.

258 The defect in myocardial function was accompanied by downregulation of numerous genes
259 associated with striated muscle differentiation, striated muscle contraction, contractile fibres,
260 regulation of heart contraction force, cardiac muscle cell action potential, and regulation of blood
261 circulation (Supplementary Fig. 10C-F), in the left ventricle and left atrium in 3.5-month-old
262 *Mhc-cre;Cdk*13$^{fl/fl}$ mice. Several important genes associated with myocardial development, such
263 as *Bmp*7, *Zfpm*1, *Hand*2, *Tbx*6, and *Dmd,* were found among the downregulated genes
264 (Supplementary Fig. 10E, F). Specifically, Bmp7 contributes to ventral body wall closure
265 (Nishimatsu and Thomsen 1998; Schmid et al. 2000; Kim et al. 2019), Zfpm1 is involved in

266 ventricular septal defects (Katz et al. 2003), Hand2 is required for cardiac gene expression and
267 outflow tract development (Holler et al. 2010; VanDusen et al. 2014), and Tbx6 is critical for
268 cardiovascular lineage diversification (Sadahiro et al. 2018). Mutation of *Dmd* is a well-known
269 genetic disease caused by the loss of functional dystrophin protein, which is responsible for the
270 stability of skeletal muscle fibres and cardiomyocytes during contraction (García-Rodríguez et al.
271 2020; Mercuri et al. 2013). The transcriptional reduction of *Dmd* was also confirmed by the
272 immunofluorescence staining in left ventricular tissues from 7-month-old *Cdk*13$^{fl/fl}$ mice
273 (Supplementary Fig. 10G). The reductions in the expression of *Dmd* and other genes in *Cdk*13$^{fl/fl}$
274 mice perfectly illustrated the myocardial dysfunction.

275 To study whether the heart defects and epigenetic gene silencing in *mhc-cre;Cdk*13$^{fl/fl}$ mice were
276 the consequence of *Cdk*13 mutation in prenatal development, *Cdk*13 was conditionally deleted in
277 postnatal mice generated by crossing *Cdk*13$^{fl/fl}$ mice with *ubc-creERT2* mice. The offspring *ubc-*
278 *creERT2;Cdk*13$^{fl/fl}$ mice, which expressed cre recombinase in most tissues after tamoxifen
279 induction for 5 days at 1 month of age, were designated *Cdk*13^{uKO} mice. After 12 months of
280 postnatal life, the *Cdk*13^{uKO} mice developed normally, with no apparent differences in heart
281 morphology, behaviour or body weight compared with those of controls (Supplementary Fig.
282 10H). The deletion efficiency of *Cdk*13 in *creERT2*;*Cdk*13$^{fl/fl}$ mice was measured using standard
283 PCR, and approximately 90% deletion was observed (Supplementary Fig. 10I). This result, along
284 with the early embryonic heart defects caused by the loss of *Cdk*13, supports that Cdk13 is a
285 critical regulator of prenatal development.

286 We next evaluated whether inhibition of H3K9me3 by GIVI can rescue the mouse heart defects
287 caused by the loss of Cdk13. *Mhc-cre;Cdk*13$^{fl/fl}$ mice at 6–7 months of age were treated with 10
288 mg/kg GIVI per day for 30 consecutive days. Immunohistological analysis of the left ventricle
289 showed a reduction in the fibrotic area in GIVI-treated *Mhc-cre;Cdk*13$^{fl/fl}$ mice (Fig. 6B). In

290 addition, the expression of *Dmd* was also elevated after GIVI treatment (Fig. 6C). Further
291 echocardiogram analysis showed that markers of left ventricle global systolic function in *Mhc-*
292 *cre;Cdk*13$^{fl/fl}$ mice, such as the left ventricular ejection fraction and left ventricular fractional
293 shortening, were significantly recovered by GIVI treatment (Fig. 6D). Notably, the survival rate
294 of GIVI-treated *Mhc-cre*;*Cdk*13$^{fl/fl}$ mice was significantly increased compared to the *Mhc-*
295 *cre*;*Cdk*13$^{fl/fl}$ group without GIVI treatment, with a maximum lifespan extended more than 40%
296 (108 days) (Fig. 6E). These results suggest that inhibiting H3K9me3 by GIVI is sufficient to
297 alleviate heart defects caused by the loss of Cdk13 and facilitates the survival rate of mutant
298 animals.

299 To confirm any changes in H3K9me3 on chromatin in GIVI-treated *Mhc-cre*;*Cdk13*$^{fl/fl}$ mice, we
300 performed ChIP quantitative PCR to examine the enrichment of H3K9me3 on the *Dmd* gene and
301 two other known key regulators of myocardial development, *Bmp*7 and *Zfpm*1. We used heart
302 tissue from *Mhc-cre*;*Cdk*13$^{fl/fl}$, GIVI-treated *Mhc-cre*;*Cdk*13$^{fl/fl}$, and control mice at E17.5 for the
303 ChIP quantitative PCR. The results showed that the elevations in H3K9me3 intensity along the
304 majority of gene bodies of *Dmd*, *Bmp*7, and *Zfpm*1 in *Mhc-cre*;*Cdk*13$^{fl/fl}$ mice were indeed
305 reduced in the presence of GIVI (Fig. 6F, Supplementary Fig. 10J), further supporting the key
306 role of H3K9me3 in *Cdk*13-congenital syndrome and suggesting that GIVI is a potential drug for
307 treating the genetic disease.

308

309

310 **Discussion**

311 There are increasing studies indicating the important role that metazoan C-terminal domain
312 (CTD) kinase members - dCDK12/Cdk12/hCDK12 and Cdk13/hCDK13 - play in transcription
313 and diseases. In the genome of fruit flies - *Drosophila melanogaster* - the orthologue is named
314 dCDK12 (Bartkowiak et al. 2010). In humans, it is known as CDK12/hCDK12 and
315 CDK13/hCDK13 (Chen et al. 2006). Several studies have reported that
316 dCDK12/CDK13/hCDK13 is involved in CTD phosphorylation at Ser2/5 (Pan et al. 2015;
317 Bartkowiak et al. 2010; Greifenberg et al. 2016), RNA polymerase II processivity or nuclear
318 RNA surveillance (Fan Z et al., Sci Adv. 2020; Insco ML et al., 2023, Science).

319 We demonstrated in this study that mice Cdk13 plays an important role in preventing
320 heterochromatin spreading. We further show that Cdk13 modulates the phosphorylation of
321 master heterochromatin regulators, including H3K9me HMTs - Suv39h2, Setdb1, and G9a - and
322 the reader of H3K9me2/3 - HP1 orthologues. The loss of specific HP1β phosphorylation at S89
323 and S91 increases the interaction between HMTs and HP1β (Fig. 4C, D). As a result, this may
324 lead to heterochromatin spreading at euchromatic genes, both in *Cdk*13-KD MEFs and *Cdk*13$^{-/-}$
325 mutant tissues, and various embryonic defects (Fig. 1, Fig. 2D-G, Fig. 6F, Supplementary Fig. 3).
326 The observation that Cdk13 mainly affected the development of prenatal mice (Supplementary
327 Fig.3C-F), but appeared to be redundant in postnatal mice (Supplementary Fig.10H),suggests a
328 temporospatial role of mice Cdk13. This is also supported by the fact that approximately 90%
329 deletion was observed in adult *creERT2*;*Cdk*13$^{fl/fl}$ mutant animals (Supplementary Fig. 10I), and
330 other phenotypic analysis with different *cre*- drivers (data not shown).

331 In conclusion, our data reveal that Cdk13 plays a critical role in a phosphorylation-based
332 mechanism for facultative H3K9me3-heterochromatin spreading in mammals. The present study

333 also suggested that H3K9me3-heterochromatin spreading is a key driver of *Cdk*13 mutation-
334 induced congenital heart syndrome. The identified GIVI has been found to relieve congenital
335 heart defects triggered by *Cdk*13 mutation, which may provide a theraputic approach for *CDK*13
336 mutation or heterochromatin alteration-induced congenital diseases.
337

Methods

Mouse usage, Embryonic development, and Morphology identification

All experiments and maintenance of mice in this study were conducted in compliance with the University of Health Guide for the Care and Use of Laboratory Animals and approved by the Biological Research Ethics Committee of Tongji University.

For mice with different gestation periods, female mice were euthanized by cervical dislocation, and their abdomens were disinfected with 70% ethanol. The uterus, full of embryos, was then removed, and individual embryos were separated from the uterine membrane. The embryos were observed and photographed under a stereomicroscope. Observation of the vaginal plug was considered Embryonic Day 0.5 (E0.5). The genetic background of wildtype and the *Cdk*13 mutant genetic background of $Cdk13^{f1/f1}$ was C57/BL6.

Cell culture

MEF/3T3 cells were cultured in Dulbecco's Modified Eagle's Medium (catalog number R10-017-CV) from Corning, NY, USA, containing 10% fetal bovine serum (catalog number 16000) from Gibco, Waltham, MA, USA, and 1% penicillin/streptomycin (catalog number SV30010) from HyClone, Logan, UT, USA. The cells were cultured in a 37 °C incubator with 5% CO2.

shRNA

The targeting sequences against the Cdk13 gene used in the present study were as follows: Cdk13 KD (5'-AGAGTATCATCAATATGAA-3') and control (5'-TTCTCCGAACGTGTCACGT-3'). They were cloned into the hU6-MCS-Ubiquitin-EGFP-IRES-puromycin vector and packaged into lentiviruses. The packaged lentiviruses harboring the shRNA vectors were then introduced into mouse embryonic fibroblasts, and flow cytometry was used to separate the GFP-positive cells to obtain stable cell lines.

Immunocytochemical staining

Mouse embryonic fibroblast cells were grown on slides until they were adherent. The cells were fixed with 4% paraformaldehyde (w/vol) for 30 min at 25 °C, and washed with phosphate-buffered saline (PBS) three times, 10 min for each. Then cells were permeabilized with 0.1% Triton-X 100 in PBS for 30 min at 25 °C, washed with PBS three times, and then blocked with a solution containing 4% bovine serum albumin for 1 h at 25 °C. Primary antibodies against HP1β (ab10478) (Abcam, Cambridge, UK), H3K9me3 (ab8898) (Abcam, Cambridge, UK), H3K4me3 (ab8580) (Abcam, Cambridge, UK), H3K9ac (ab10812, Cambridge, UK), H3K27ac (ab4729, Cambridge, UK), Trim28 (ab109287, Cambridge, UK) and H4K16ac (cs204361, Millipore, USA) were added, and the cells were incubated at 4 °C overnight. The cells were then washed with PBS three times.

A secondary antibody solution was dropped onto the cells, and they were incubated for 1 hour at 25 °C in the dark. Then, the cells were washed with PBS three times. DAPI (5 μg/ml) was added, and the cells were incubated at room temperature in the dark for 10 minutes. The cells were then washed three times in PBS. Finally, anti-fluorescence quenching agent was added to the slides to seal them, and fluorescence photographs were taken.

Transmission electron microscopy

*Cdk*13 KD and control mouse embryonic fibroblast cells were digested with 0.125% trypsin. The digestion was blocked with serum, and the cells were centrifuged at 350 g for 5 min. The cell pellets were fixed with 2.5% glutaraldehyde in PBS (0.1 M phosphate buffer, pH7.4) for 30 min at 25˚C. The cell precipitates were embedded and sectioned following standard procedure, and were examined under transmission electron microscopy.

Preparation of tissue into paraffin sections

Freshly removed tissues were washed with PBS to remove blood, the 4% paraformaldehyde equal to the 20-fold volume that of tissue was added, and the tissues were fixed at 4 °C overnight. After washing with PBS three times, 70% ethanol was added, and the tissues were allowed to dehydrate overnight. The tissues were placed in an embedding box and dehydrated in a gradient of 80% ethanol, 90% ethanol, 95% ethanol I, 95% ethanol II, 100% ethanol I and 100% ethanol II for 30 min per concentration. The embedding box was placed in xylene II and xylene I for 3 min each. The embedding box was then placed in benzene wax, wax I, wax II and wax III for 30 min in sequence at 60 °C. After embedding, the tissue blocks were placed on a -20 °C cold table for at least 1 h. After solidification, paraffin sections with a thickness of 5 μm were prepared using a slicer. After spreading on a 42 °C slide machine, the sections were placed onto slides and incubated in a 37 °C oven overnight.

Immunofluorescence staining of paraffin sections

The paraffin sections were placed in xylene I and xylene II for 5 min, and sequentially placed in 100% ethanol I, 100% ethanol II, 95% ethanol I, 95% ethanol II, 90% ethanol, 80% ethanol, 70% ethanol, ddH_2O and PBS for 2 min each. The slides were placed in preheated sodium citrate (pH = 6.0) for 20 min at 97 °C. The slides were washed with PBS after the temperature dropped to 25 °C. Bovine serum albumin was dropped onto the slides, which were then left to stand at room temperature for 1 h. Primary antibodies against HP1β (ab10478) (Abcam, Cambridge, UK), HP1γ (ABE1329) (Millipore, Burlington, MA, USA), H3K9me3 (ab8898) (Abcam, Cambridge, UK), Trim28 (ab109287) (Abcam, Cambridge, UK), Ki67 (ab16667, Cambridge, UK), RNA polymerase II p-Ser2 (ab5095, Cambridge, UK), RNA polymerase II p-Ser5 (ab5131, Cambridge, UK) Dmd (ab15277) (Abcam, Cambridge, UK), and cTnt (MA5-12960) (Invitrogen, Waltham, MA, USA) were added, and the slides were incubated overnight at 4 °C before washing three times by PBS. The secondary antibody solution was dropped onto the slides, which were incubated for 1 h at room temperature in the dark and then washed with PBS three times. DAPI (5 μg/ml) was added onto the slides and incubated at room temperature under dark for 10 min,

419 then washed in PBS three times. Anti-fluorescence quenching agent was dropped onto the slides
420 to seal them, and then fluorescence photographs were taken.
421
422 **Haematoxylin and eosin staining**
423 The paraffin sections were placed in xylene I and xylene II for 5 min and then sequentially
424 incubated in 100% ethanol I, 100% ethanol II, 95% ethanol I, 95% ethanol II, 90% ethanol, 80%
425 ethanol, 70% ethanol, and ddH_2O for 2 min each. The sections were then washed with ddH_2O
426 three times. The sections were soaked in haematoxylin staining solution for 30 s, rinsed with
427 ddH_2O, soaked in 1% acetic acid for 30 s, rinsed with ddH_2O, soaked in eosin staining solution
428 for 2 min, and then rinsed with ddH_2O. The sections were placed in 95% ethanol III, 95%
429 ethanol IV, 100% ethanol III and 100% ethanol IV for 2 min each in sequence for dehydration.
430 The sections were placed in xylene III and xylene IV for 5 min each in sequence, sealed with
431 neutral gum and left to dry.
432
433 **Masson staining**
434 The paraffin sections were sequentially placed in xylene I and xylene II, each for 5 minutes;
435 100% ethanol I and 100% ethanol II, 95% ethanol I and 95% ethanol II, 90% ethanol, 80%
436 ethanol, 70% ethanol, and ddH_2O for 2 minutes each, and then washed with ddH_2O three times.
437 The sections were soaked in Bouin's staining solution and washed with ddH_2O after incubation
438 in a 56 °C bath for 15 minutes. Then, the sections were soaked in haematoxylin staining solution
439 for 1 minute, rinsed with ddH_2O, soaked in eosin staining solution for 30 seconds, and rinsed
440 with ddH_2O. The sections were then incubated in phosphomolybdic acid separation solution for 8
441 minutes and in aniline blue staining solution for 5 minutes before being rinsed with 1% acetic
442 acid in ddH_2O.
443
444 To dehydrate the sections, they were placed in 95% ethanol III and 95% ethanol IV, 100%
445 ethanol III, and 100% ethanol IV for 2 minutes each. They were then placed in xylene III and
446 xylene IV for 5 minutes each, sealed with neutral gum, and left to dry.
447
448 **Coimmunoprecipitation analysis**
449 Mouse embryonic fibroblasts were collected and washed with ice-cold PBS, resuspended in
450 RIPA lysis buffer (containing 25 mM Tris-Cl, pH 7.5; 150 mM NaCl; 1% NP-40; 1% sodium
451 deoxycholate; 0.1% SDS; 1x protein cocktail; and 1 mM PMSF) and sonicated on ice for 4 min
452 by 12% efficiency. The cell lysates were incubated with protein A/G beads (sc-2003) (Santa
453 Cruz Biotechnology, Dallas, TX, USA) for 30 min to eliminate the background signal, and then
454 incubated with anti-HP1α (NB110-40623) (Novus, St Louis, MO, USA) or GFP-Trap (gta-20)
455 (Chromotek, Germany) antibodies at 4 °C overnight. The next day, for anti-HP1α binding, the
456 samples were incubated in protein A/G agarose beads solution for 2 h. Then, the samples were
457 centrifuged to harvest the agarose beads, and the beads were washed three times with
458 immunoprecipitation buffer (20 mM HEPES, pH 8.0; 0.2 mM EDTA; 5% glycerol; 150 mM
459 NaCl; and 1% NP-40). The precipitated proteins were released by boiling in loading buffer and

separated by SDS–PAGE (10%). Immunoblot analyses were performed with antibodies against G9a (3306) (CST, Walall, UK), SUV39H2 (ab240313) (Abcam, Cambridge, UK), SETDB1 (A6145) (Abclonal, Woburn, MA, USA), HP1α (NB110-40623) (Novus, St Louis, MO, USA), HP1β (MAC-053) (Thermo Fisher, Waltham, MA, USA), HDAC3 (A16462, Woburn, MA, USA) and HP1γ (MAC-054) (Thermo Fisher, Waltham, MA, USA).

RNA sequencing

Two micrograms of RNA were obtained and delivered to Novogene Company for RNA quality inspection, library construction and sequencing. The library type was a eukaryotic common transcriptome library (250-300 bp), the sequencing machine model was a HiSeq X Ten, the mode was PE150, and 9 GB of original data were obtained for each sample.

The sequencing files were mapped to the mouse genome mm10 using HISAT2 (v2.1.0) (Kim et al. 2015), and featureCounts (v1.6.2) (Liao et al. 2014) was used to obtain a gene expression matrix from the mapped reads. DESeq2 (v1.30.0) (Love et al. 2014) was used to identify differentially expressed genes (DEGs) with the LRT test. DEGs (differentially expressed genes) were defined as genes with an absolute fold change greater than 1.3 and an adjusted p-value less than 0.1. ClusterProfiler (v3.18.0) (Yu et al. 2012) and org.Mm.eg.db (v3.12.0) (Carlson et al. 2010) were used to perform Gene Ontology enrichment analysis.

Chromatin immunoprecipitation assay

Mouse embryonic fibroblasts or mouse embryonic heart tissues were digested into single cells and washed with ice-cold PBS. The cells were incubated with 1% formaldehyde in PBS for 10 min, quenched with 0.125 M glycine, and washed twice with ice-cold PBS. The cell pellets were resuspended in ice-cold lysis buffer (50 mM Tris-Cl, pH 8.0; 140 mM NaCl; 1 mM EDTA; 10% glycerol; 0.5% NP-40; 0.25% Triton X-100; 1x protein cocktail), incubated on ice for 20 min, transferred to a prechilled Dounce homogenizer and homogenized. The nuclei were harvested by centrifugation, resuspended in nuclear lysis buffer (50 mM Tris-Cl, pH 8.0; 10 mM EDTA; 1% SDS; 1x protein cocktail) and incubated on ice for 20 min. The samples were sonicated on high power with 30s on and 30s off for a total 60 min. The solution of sheared chromatin was harvested and diluted with dilution buffer (50 mM Tris-Cl, pH 7.4; 150 mM NaCl; 1 mM EDTA; 1% NP-40, 0.25% deoxycholic acid). Then, 10 μg of anti-H3K9me3 antibody (ab8898) (Abcam, Cambridge, UK) was added, and the samples were incubated on a rotator overnight at 4 °C. Magnetic protein G beads (9006) (CST Pharma, Walsall, UK) were added, and the solution was incubated for 4 h. Then, the beads were harvested with a magnet and washed three times with wash buffer (100 mM Tris-Cl, pH 8.0; 500 mM LiCl; 1% NP-40; 1% deoxycholic acid; 1x protein cocktail). DNA was eluted with elution buffer (50 mM $NaHCO_3$, 1% SDS) and extracted with a DNA purification kit. The eluted DNA was subjected to high-throughput sequencing or quantitative polymerase chain reaction.

501 For sequencing, DNA library construction and sequencing were performed by GENEWIZ
502 Company. The sequencing files were mapped to the mouse genome mm10 using Bowtie2 (v2.4.2)
503 (Langmead and Salzberg 2012) with the parameters --no-unal --no-mixed --no-discordant. The
504 unmapped reads were filtered with samtools (v1.3.1) (Li et al. 2009) view with the parameters -F
505 12 -q 10, and duplicated reads were removed with sambamba (v0.8.1) (Tarasov et al. 2015)
506 markdup. Mitochondrial DNA and blacklist regions were also removed. Macs2 (v2.2.7.1) (Zhang
507 et al. 2008) was used for peak calling with the parameters -g mm -q 0.05 --broad -f BAMPE. The
508 BAM files were converted into bigwig files using bamCoverage from deepTools (v3.5.1)
509 (Ramirez et al. 2016) with the parameter -bs 10 --normalizeUsing RPKM. Signals around the
510 TSS (±3 kb) were calculated and visualized with computeMatrix. The bigwig files were
511 compared using bigwigCompare with -bs 10. The packages ChIPseeker (v1.22.1) (Yu et al. 2015)
512 and TxDb.Mmusculus. UCSC.mm10.knownGene (v3.10.0) was used to annotate peaks. The
513 protocols for Gene Ontology enrichment analysis were similar to those for RNA sequencing
514 analysis.
515
516 Quantitative reverse transcription-polymerase chain reaction (qRT–PCR) of H3K9me3 ChIP
517 DNA was run in a Roche Light Cycler 96 thermocycler as follows: one cycle of 95 °C for 1 min;
518 40 cycles of 95 °C for 1 min, 60 °C for 1 min, and 72 °C for 1 min; and one cycle of 72 °C for 5
519 min. The data from the immunoprecipitates were normalized with the data from the 1% input
520 samples. Please see the supplementary material for the primer sequence
521
522 **Echocardiography in mice**
523 Cardiac function was evaluated using a high-resolution small-animal ultrasound imaging system
524 (Vevo2100). Mice were anaesthetized with 1% isoflurane until the heart rate stabilized at 400–
525 500 beats per min. Seven parasternal long-axis images were obtained in B mode and scanned
526 appropriately to determine the maximum left ventricular length. In this view, the M-mode cursor
527 was perpendicular to the maximum left ventricular size at the end diastolic and systolic stages,
528 and M-mode images were obtained to measure the wall thickness and chamber size.
529
530 **Treatment of cells and mice with small molecule drugs**
531 For the cell experiment, the small molecule drugs were dissolved in DMSO to different
532 concentration as a stock solution. The stock solution was added to *Cdk*13 KD mouse 3T3 cell
533 growth medium in a final concentration (See Supplementary Table 3), and the cells were
534 incubated for 72 h, then immunofluorescence experiments were performed.
535
536 For animal experiments, GIVI was dissolved in DMSO to 20 mg/ml and prepared as a stock
537 solution. The 1 mg/ml working solution containing of 5% GIVI (stock solution), 40% PEG300,
538 5% Tween 80, and 50% ddH_2O. The control solution containing of 5% DMSO, 40% PEG300,
539 5% Tween 80 and 50% ddH_2O. Then, mice were given intraperitoneal injections of control and
540 GIVI (10 mg/kg/day) solutions for 30 days.
541

542 **Protein phosphorylation mass spectrometry**
543 Mouse embryonic fibroblasts, including *Cdk*13 knockdown (*Cdk*13 KD) and control cells
544 (Control), were harvested (109 cells for each sample) and washed twice with PBS. Then, the
545 samples were sonicated on ice for three minutes using a high-intensity ultrasonic processor
546 (Scientz) in lysis buffer (8 M urea, 1% protease inhibitor cocktail). The remaining debris was
547 removed by centrifugation at 12,000 g at 4°C for ten minutes. Finally, the supernatant was
548 collected, and the protein concentration was determined using a BCA kit according to the
549 manufacturer's instructions. The sample was slowly added to the final concentration of 20% (m/v)
550 TCA to precipitate protein, then mixed by vertexing and incubated for two hours at 4°C. The
551 precipitate was collected by centrifugation at 4500 g for five minutes at 4°C. The precipitated
552 protein was washed with pre-cooled acetone three times and dried for one minute. The protein
553 sample was then redissolved in 200 mM TEAB and ultrasonically dispersed. Trypsin was added
554 at a 1:50 trypsin-to-protein mass ratio for the first digestion overnight. The sample was reduced
555 with 5 mM dithiothreitol for 60 minutes at 37°C and alkylated with 11 mM iodoacetamide for 45
556 minutes at room temperature in the darkness. Finally, the peptides were desalted using a Strata X
557 SPE column.
558
559 Peptide mixtures were first incubated with IMAC microsphere suspension and vibrated in
560 loading buffer (50% acetonitrile/0.5% acetic acid). To remove the non-specifically adsorbed
561 peptides, the IMAC microspheres were washed sequentially with 50% acetonitrile/0.5% acetic
562 acid and 30% acetonitrile/0.1% trifluoroacetic acid. To elute the enriched phosphopeptides, the
563 elution buffer containing 10% NH_4OH was added, and the enriched phosphopeptides were eluted
564 with vibration. The supernatant containing phosphopeptides was collected and lyophilized for
565 LC-MS/MS analysis.
566
567 The tryptic peptides were dissolved in solvent A (0.1% formic acid, 2% acetonitrile/ in water)
568 and directly loaded onto a homemade reversed-phase analytical column (25 cm length, 100 μm
569 i.d.). Peptides were separated with a gradient from 3% to 20% solvent B (0.1% formic acid in
570 90% acetonitrile) over 70 minutes, 20% to 30% in 12 minutes, and climbing to 80% in four
571 minutes, then holding at 80% for the last four minutes, all at a constant flow rate of 500 nL/min
572 on an EASY-nLC 1200 UPLC system (Thermo Fisher Scientific).
573
574 The separated peptides were analyzed in an Orbitrap ExplorisTM 480 (Thermo Fisher Scientific)
575 with a nano-electrospray ion source. The electrospray voltage applied was 2.3 kV. The full MS
576 scan resolution was set to 60,000 for a scan range of 400 -1200 m/z. Up to 15 most abundant
577 precursors were then selected for further MS/MS analyses with 30 s dynamic exclusion. The
578 HCD fragmentation was performed at a normalized collision energy (NCE) of 27%. The
579 fragments were detected in the Orbitrap at a resolution of 30,000. Fixed first mass was set as 110
580 m/z. Automatic gain control (AGC) target was set at 75% with an intensity threshold of 2E4 and
581 a maximum injection time of 100 ms.
582

583 **Protein phosphorylation data analysis**
584 The resulting MS/MS data were processed using the Proteome Discoverer search engine
585 (v2.4.1.15). Tandem mass spectra were searched against the Mus musculus SwissProt database
586 (17,063 entries), concatenated with a reverse decoy database. Trypsin (full) was specified as the
587 cleavage enzyme, allowing up to two missing cleavages. The mass tolerance for precursor ions
588 was set to 10 ppm in the first search and the mass tolerance for fragment ions was set to 0.02 Da.
589 Carbamidomethyl on Cys was specified as the fixed modification, and acetylation on protein N-
590 terminal, oxidation on Met, deamidation (NQ), and phosphorylation on Ser, Thr, and Tyr were
591 specified as variable modifications. The FDR was adjusted to <1%. All the other parameters in
592 the Proteome Discoverer were set to default values.
593
594 The raw LC-MS datasets were first searched against the database and converted into matrices
595 containing the intensity of peptides across samples. The relative quantitative and statistical
596 values of each modified peptide were then calculated based on this intensity information by the
597 following steps:
598
599 1. Peptides with a modification pattern described as "positions not distinguishable" and Quan
600 Info marked by "NoQuanValues" were removed from all peptide datasets.
601
602 2. The intensities of modified peptides (I) were centralized and transformed into relative
603 quantitative values (R) of modified peptides in each sample using the following formula: Rij = Iij
604 / Mean(Ij). Here, i denotes the sample and j denotes the modified peptide. If both proteomics and
605 post-translational modification profiling were conducted on the same cohort, the relative
606 quantitative value of the modified peptide was typically divided by the relative quantitative value
607 of the corresponding protein to remove the influence from protein expression of modifications.
608
609 3. Average relative quantitative values were calculated for each group, and the log2 ratio values
610 of *Cdk*13 KD compared with control groups were also calculated.
611
612 4. P-values were calculated with log2 relative quantitative values using a t-test. The modified
613 sites with |fold change | > 1.5 and P < 0.1 were regarded as differentially expressed
614 phosphopeptides. Gene Ontology enrichment analysis was carried out using a method similar to
615 that used for RNA-seq analysis.
616
617
618 **Software**
619 HISAT2 v2.1.0
620 featureCounts v1.6.2
621 R v4.0.3
622 DESeq2 v1.30.0
623 clusterProfiler v3.18.0

org.Mm.eg.db v3.12.0
Bowtie2 v2.4.2
samtools v1.3.1
sambamba v0.8.1
macs2 v2.2.7.1
deepTools v3.5.1
ChIPseeker v1.22.1
TxDb.Mmusculus.UCSC.mm10.knownGene v3.10.0
ggplot2 v3.3.5
pheatmap v1.0.12
UCSC genome browser http://genome.ucsc.edu
GraphPad Prism 8 version 8.3.0(538)
mm10-blacklist.v2
Cytoscape 3.8.0
MoMo Version 5.4.1 https://meme-suite.org/meme/tools/momo

641 **References**

642 Allshire, R. C. & Madhani, H. D. Ten principles of heterochromatin formation and function. Nat
643 Rev Mol Cell Biol 19, 229–244 (2018).
644 Bartkowiak, B. et al. CDK12 is a transcription elongation-associated CTD kinase, the metazoan
645 ortholog of yeast Ctk1. Genes Dev. 24, 2303–2316 (2010).
646 Becker, J. S. et al. Genomic and Proteomic Resolution of Heterochromatin and Its Restriction of
647 Alternate Fate Genes. Molecular Cell 68, 1023-1037.e15 (2017).
648 Bösken, C. A. et al. The structure and substrate specificity of human Cdk12/Cyclin K. Nat
649 Commun 5, 3505 (2014).
650 Bostwick, B. L. et al. Phenotypic and molecular characterisation of CDK13-related congenital
651 heart defects, dysmorphic facial features and intellectual developmental disorders. Genome
652 Med 9, 73 (2017).
653 Carlson, M. org.Mm.eg.db: Genome wide annotation for Mouse. R package version 3.12.0.
654 (2020).
655 Chalamcharla, V. R., Folco, H. D., Dhakshnamoorthy, J. & Grewal, S. I. S. Conserved factor
656 Dhp1/Rat1/Xrn2 triggers premature transcription termination and nucleates heterochromatin
657 to promote gene silencing. Proc. Natl. Acad. Sci. U.S.A. 112, 15548–15555 (2015).
658 Chen, H.-H., Wang, Y.-C. & Fann, M.-J. Identification and Characterization of the
659 CDK12/Cyclin L1 Complex Involved in Alternative Splicing Regulation. Mol. Cell. Biol.
660 26, 2736–2745 (2006).
661 Chen, H.-H., Wong, Y.-H., Geneviere, A.-M. & Fann, M.-J. CDK13/CDC2L5 interacts with L-
662 type cyclins and regulates alternative splicing. Biochemical and Biophysical Research
663 Communications 354, 735–740 (2007).
664 Dai, Q. et al. Cyclin K-containing Kinase Complexes Maintain Self-renewal in Murine
665 Embryonic Stem Cells. Journal of Biological Chemistry 287, 25344–25352 (2012).
666 Deciphering Developmental Disorders Study. Prevalence and architecture of de novo mutations
667 in developmental disorders. Nature 542, 433–438 (2017).
668 Eissenberg, J. C. & Elgin, S. C. R. HP1a: a structural chromosomal protein regulating
669 transcription. Trends Genet 30, 103–110 (2014).
670 Even, Y. et al. CDC2L5, a Cdk-like kinase with RS domain, interacts with the ASF/SF2-
671 associated protein p32 and affects splicing in vivo. J. Cell. Biochem. 99, 890–904 (2006).
672 Fan, Z., Devlin, J.R., Hogg, S.J., Doyle, M.A., Harrison, P.F., Todorovski, I., Cluse, L.A.,
673 Knight, D.A., Sandow, J.J., Gregory, G., et al. (2020). CDK13 cooperates with CDK12 to
674 control global RNA polymerase II processivity. Sci. Adv. 6.
675 Fischle, W., Wang, Y. & Allis, C. D. Binary switches and modification cassettes in histone
676 biology and beyond. Nature 425, 475–479 (2003).
677 García-Rodríguez, R. et al. Premature termination codons in the DMD gene cause reduced local
678 mRNA synthesis. Proc. Natl. Acad. Sci. U.S.A. 117, 16456–16464 (2020).
679 Greifenberg, A. K. et al. Structural and Functional Analysis of the Cdk13/Cyclin K Complex.
680 Cell Reports 14, 320–331 (2016).
681 Grewal, S. I. S. & Jia, S. Heterochromatin revisited. Nat Rev Genet 8, 35–46 (2007).
682 Hall, I. M. et al. Establishment and Maintenance of a Heterochromatin Domain. Science 297,
683 2232–2237 (2002).
684 Hamilton, M. J. & Suri, M. CDK13-related disorder. Adv Genet 103, 163–182 (2019).
685 Hiriart, E. et al. Mmi1 RNA surveillance machinery directs RNAi complex RITS to specific
686 meiotic genes in fission yeast: Targeting RITS to meiotic RNAs and genes. The EMBO

687 Journal 31, 2296–2308 (2012).
688 Holler, K. L. et al. Targeted deletion of Hand2 in cardiac neural crest-derived cells influences
689 cardiac gene expression and outflow tract development. Developmental Biology 341, 291–
690 304 (2010).
691 Insco, M.L., Abraham, B.J., Dubbury, S.J., Kaltheuner, I.H., Dust, S., Wu, C., Chen, K.Y., Liu,
692 D., Bellaousov, S., Cox, A.M., et al. (2023). Oncogenic CDK13 mutations impede nuclear
693 RNA surveillance. Science 380, eabn7625.
694 Jenuwein, T. & Allis, C. D. Translating the Histone Code. Science 293, 1074–1080 (2001).
695 Ji, H. et al. HDAC3 deficiency promotes liver cancer through a defect in H3K9ac/H3K9me3
696 transition. Cancer Res. 79, 3676–3688 (2019).
697 Katz, S. G. et al. Endothelial lineage-mediated loss of the GATA cofactor Friend of GATA 1
698 impairs cardiac development. Proc. Natl. Acad. Sci. U.S.A. 100, 14030–14035 (2003).
699 Kim, D., Langmead, B. & Salzberg, S. L. HISAT: a fast spliced aligner with low memory
700 requirements. Nat Methods 12, 357–360 (2015).
701 Kim, H.-S., Neugebauer, J., McKnite, A., Tilak, A. & Christian, J. L. BMP7 functions
702 predominantly as a heterodimer with BMP2 or BMP4 during mammalian embryogenesis.
703 Elife 8, e48872 (2019).
704 Langmead, B. & Salzberg, S. L. Fast gapped-read alignment with Bowtie 2. Nat Methods 9,
705 357–359 (2012).
706 Lee, N. N. et al. Mtr4-like Protein Coordinates Nuclear RNA Processing for Heterochromatin
707 Assembly and for Telomere Maintenance. Cell 155, 1061–1074 (2013).
708 Li, H. et al. The Sequence Alignment/Map format and SAMtools. Bioinformatics 25, 2078–2079
709 (2009).
710 Liang, K. et al. Characterization of Human Cyclin-Dependent Kinase 12 (CDK12) and CDK13
711 Complexes in C-Terminal Domain Phosphorylation, Gene Transcription, and RNA
712 Processing. Mol Cell Biol 35, 928–938 (2015).
713 Liao, Y., Smyth, G. K. & Shi, W. featureCounts: an efficient general purpose program for
714 assigning sequence reads to genomic features. Bioinformatics 30, 923–930 (2014).
715 Love, M. I., Huber, W. & Anders, S. Moderated estimation of fold change and dispersion for
716 RNA-seq data with DESeq2. Genome Biol 15, 550 (2014).
717 Mercuri, E. & Muntoni, F. Muscular dystrophy: new challenges and review of the current
718 clinical trials. Current Opinion in Pediatrics 25, 701–707 (2013).
719 Moazed, D. Mechanisms for the Inheritance of Chromatin States. Cell 146, 510–518 (2011).
720 Nicetto, D. & Zaret, K. S. Role of H3K9me3 heterochromatin in cell identity establishment and
721 maintenance. Curr Opin Genet Dev 55, 1–10 (2019c).
722 Nicetto, D. et al. H3K9me3-heterochromatin loss at protein-coding genes enables developmental
723 lineage specification. Science 363, 294–297 (2019).
724 Nishimatsu, S. & Thomsen, G. H. Ventral mesoderm induction and patterning by bone
725 morphogenetic protein heterodimers in Xenopus embryos. Mechanisms of Development 74,
726 75–88 (1998).
727 Nováková, M., Hampl, M., Vrábel, D., Procházka, J., Petrezselyová, S., Procházková, M.,
728 Sedláček, R., Kavková, M., Zikmund, T., Kaiser, J., et al. (2019). Mouse Model of
729 Congenital Heart Defects, Dysmorphic Facial Features and Intellectual Developmental
730 Disorders as a Result of Non-functional CDK13. Front. Cell Dev. Biol. 7.
731 Pan, L. et al. Heterochromatin remodeling by CDK12 contributes to learning in Drosophila. Proc.
732 Natl. Acad. Sci. U.S.A. 112, 13988–13993 (2015).
733 Ramírez, F. et al. deepTools2: a next generation web server for deep-sequencing data analysis.
734 Nucleic Acids Res 44, W160–W165 (2016).

735 Riddle, N. C. & Elgin, S. C. R. The Drosophila Dot Chromosome: Where Genes Flourish Amidst
736 Repeats. Genetics 210, 757–772 (2018).
737 Sadahiro, T. et al. Tbx6 Induces Nascent Mesoderm from Pluripotent Stem Cells and Temporally
738 Controls Cardiac versus Somite Lineage Diversification. Cell Stem Cell 23, 382-395.e5
739 (2018).
740 Schmid, B. et al. Equivalent genetic roles for bmp7/snailhouse and bmp2b/swirl in dorsoventral
741 pattern formation. Development 127, 957–967 (2000).
742 Shi, Y. J. et al. Regulation of LSD1 histone demethylase activity by its associated factors. Mol.
743 Cell 19, 857–864 (2005).
744 Shinkai, Y. & Tachibana, M. H3K9 methyltransferase G9a and the related molecule GLP. Genes
745 and Development 25, 781–788 (2011).
746 Sifrim, A. et al. Distinct genetic architectures for syndromic and nonsyndromic congenital heart
747 defects identified by exome sequencing. Nat Genet 48, 1060–1065 (2016).
748 Tarasov, A., Vilella, A. J., Cuppen, E., Nijman, I. J. & Prins, P. Sambamba: fast processing of
749 NGS alignment formats. Bioinformatics 31, 2032–2034 (2015).
750 Tashiro, S., Asano, T., Kanoh, J. & Ishikawa, F. Transcription-induced chromatin association of
751 RNA surveillance factors mediates facultative heterochromatin formation in fission yeast.
752 Genes Cells 18, 327–339 (2013).
753 van den Akker, W. M. R. et al. De novo variants in CDK13 associated with syndromic ID/DD:
754 Molecular and clinical delineation of 15 individuals and a further review. Clin Genet 93,
755 1000–1007 (2018).
756 VanDusen, N. J. et al. Hand2 Is an Essential Regulator for Two Notch-Dependent Functions
757 within the Embryonic Endocardium. Cell Reports 9, 2071–2083 (2014).
758 Volpe, T. A. et al. Regulation of Heterochromatic Silencing and Histone H3 Lysine-9
759 Methylation by RNAi. Science 297, 1833–1837 (2002).
760 Wu, Y.-M. et al. Inactivation of CDK12 Delineates a Distinct Immunogenic Class of Advanced
761 Prostate Cancer. Cell 173, 1770-1782.e14 (2018).
762 Yamanaka, S. et al. RNAi triggered by specialized machinery silences developmental genes and
763 retrotransposons. Nature 493, 557–560 (2013).
764 Yu, G., Wang, L.-G. & He, Q.-Y. ChIPseeker: an R/Bioconductor package for ChIP peak
765 annotation, comparison and visualization. Bioinformatics 31, 2382–2383 (2015).
766 Yu, G., Wang, L.-G., Han, Y. & He, Q.-Y. clusterProfiler: an R package for comparing
767 biological themes among gene clusters. OMICS 16, 284–287 (2012).
768 Zhang, Y. et al. Model-based Analysis of ChIP-Seq (MACS). Genome Biol 9, R137 (2008).
769 Zofall, M. et al. RNA Elimination Machinery Targeting Meiotic mRNAs Promotes Facultative
770 Heterochromatin Formation. Science 335, 96–100 (2012).
771
772

Data availability

All genomic data are being made accessible at the Gene Expression Omnibus (GEO) database repository. ChIP-seq: GSE190679; RNA-seq: GSE190781, GSE190692, GSE190683. Phosphoproteomic data are being made accessible at the PRoteomics IDEntifications database (PRIDE) (https://www.ebi.ac.uk/pride) repository PXD030231.

Acknowledgements We thank Professor An-Dong Qiu for generously providing us with cre mouse strains as gifts and for his helpful suggestions during the study. Professor Ci-Zhong Jiang and his group members generously helped with our bioinformatic analysis. We also thank Da-De Song and Dr Feng Sun for their technical assistance. We would also like to thank Professor Zhi-Yong Mao for his helpful suggestions during the study.

Funding

The study was funded by the Chinese Ministry of Science and Technology National Key Basic Research Project Grants 2022YFA1103703 and 2017YFA0103300 awarded to F.L.S., and a Tsingtao Municipal Government Research Grant also awarded to F.L.S.

Author contributions C.W., W.Z., X.L.C., W.F.W., X.B.G., J.F.C., Y.B.L., K.L., Y.Y.J., X.Y.L. and Y.T.L. conducted the experiments; Y.H.L. performed the bioinformatic analysis; C.W. performed the ChIP-seq preparation, ChIP–qPCR, and IP experiments; W.Z. and Y.Y.J. helped with the KO mice and immunofluorescence (IF) experiments; W.F.W., X.B.G. and K.L. helped with cell line preparation and IF staining; X.L.C. and Y.B.L. helped with myocardial-specific deletion work in mice; J.F.C. produced the mutant plasmid and performed protein interaction analysis; and W.F.W. assisted in preparing the graphics for the manuscript.

Competing interests

The authors declare no competing interests.

Additional information

Correspondence and requests for materials should be addressed to Fang-Lin Sun

Fig. 1

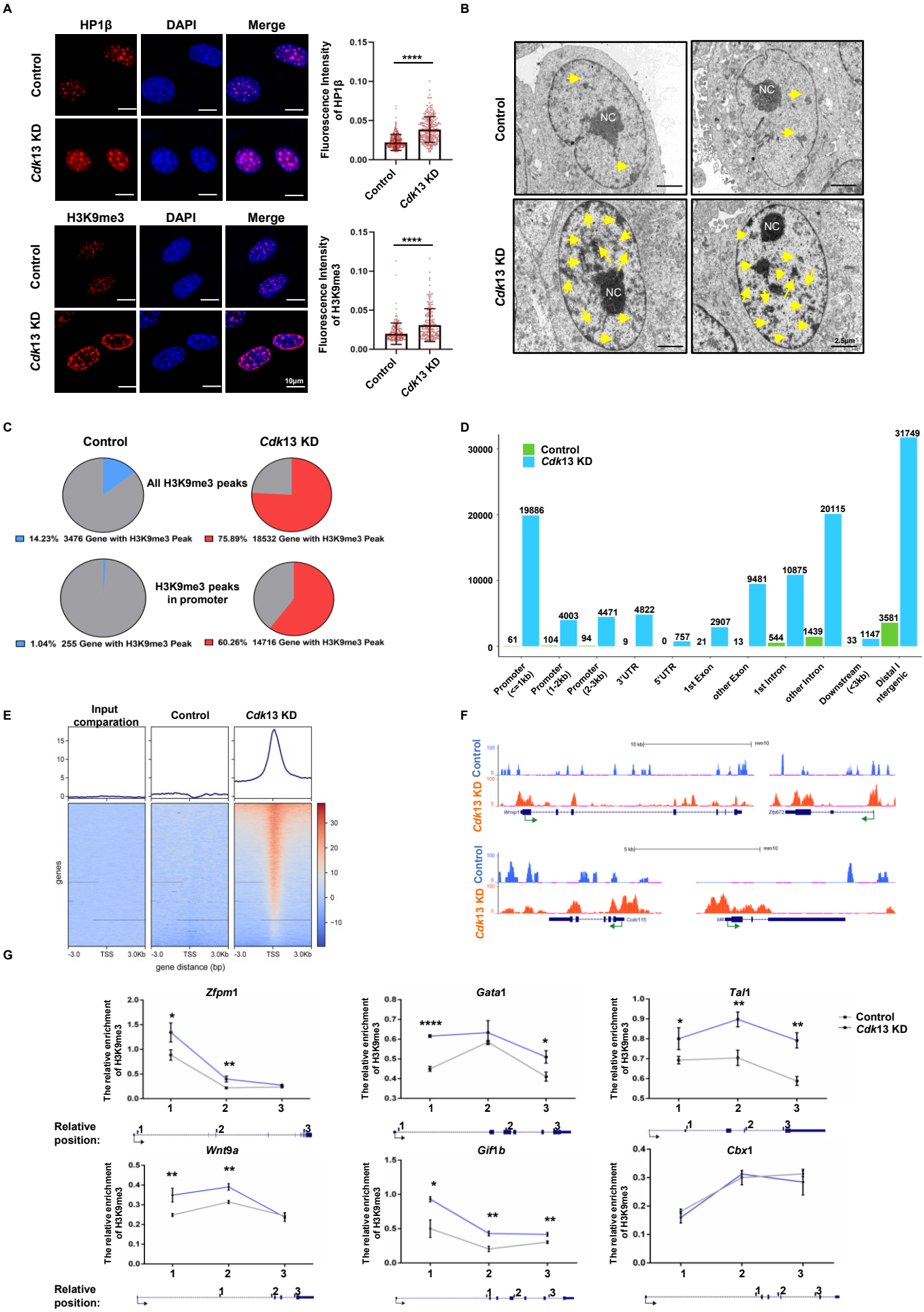
A
HP1β
DAPI
Merge
Control
Cdk13 KD
Fluorescence Intensity of HP1β
****
H3K9me3
Fluorescence Intensity of H3K9me3
10μm
B
NC
2.5μm
C
Control
Cdk13 KD
All H3K9me3 peaks
14.23% 3476 Gene with H3K9me3 Peak
75.89% 18532 Gene with H3K9me3 Peak
H3K9me3 peaks in promoter
1.04% 255 Gene with H3K9me3 Peak
60.26% 14716 Gene with H3K9me3 Peak
D
Control
Cdk13 KD
Promoter (<=1kb)
Promoter (1-2kb)
Promoter (2-3kb)
3'UTR
5'UTR
1st Exon
other Exon
1st Intron
other Intron
Downstream (<3kb)
Distal Intergenic
E
Input comparation
Control
Cdk13 KD
genes
gene distance (bp)
F
Control
Cdk13 KD
G
Zfpm1
Gata1
Tal1
Wnt9a
Gif1b
Cbx1
The relative enrichment of H3K9me3
Relative position:

810 **Fig. 1 | Global increase in H3K9me3-heterochromatinization after *Cdk*13 depletion.**
811 **A**, Left, Representative immunofluorescence staining for HP1β (red) and H3K9me3 (red) in
812 control and *Cdk*13 knockdown (KD) mouse embryonic fibroblasts (MEFs) with lentivirus
813 shRNA. Right, Quantification of fluorescence intensity of HP1β and H3K9me3. Each point
814 represents a cell, and more than 300 cells per condition were analyzed. The data are presented as
815 the means ± SEMs. ***$P < 0.001$, ****$P < 0.0001$, t test. **B**, Representative transmission electron
816 microscopy images of *Cdk*13 KD MEFs and control MEFs are shown. Fifteen nuclei were
817 analysed from each group, with arrow indicating the condensed heterochromatin. NC, nucleolus
818 **C**, The H3K9me3 globally increased in *Cdk*13 KD MEFs compared to controls. The Pie plot
819 shows the percentage of genes with H3K9me3 peaks; Above: The number and percentage of
820 genes with H3K9me3 peaks among the known genes in the entire mouse genome; Below: The
821 number and percentage of genes with H3K9me3 peaks in the promoter region (transcriptional
822 start site ± 3 kb) among the H3K9me-enriched genes before (Control) and after *Cdk*13 KD. Blue
823 represents the percentage in the control group, while red represents the percentage in the *Cdk*13
824 KD group. **D**, The enrichment of H3K9me3 peaks in all regions of euchromatic genes and
825 intergenic regions. **E**, H3K9me3 dramatically increased in *Cdk*13 KD MEFs around
826 transcriptional start sites (TSS). **F**, Representative genes with increased H3K9me3 after *Cdk*13
827 depletion are shown. The views of H3K9me3 in the UCSC genome are indicated. Blue
828 represents control group, and Red represents *Cdk*13 KD group. TSS and the direction of
829 transcription is indicated by arrows. **G**, ChIP-qPCR analysis confirmed the H3K9me3
830 enrichments in *Cdk*13 KD MEF cells compared to control cells (Control). The HP1β gene was
831 used as a negative control. Three pairs of primers, within or adjacent to the gene exon, were
832 designed for each gene.
833
834

Fig. 2

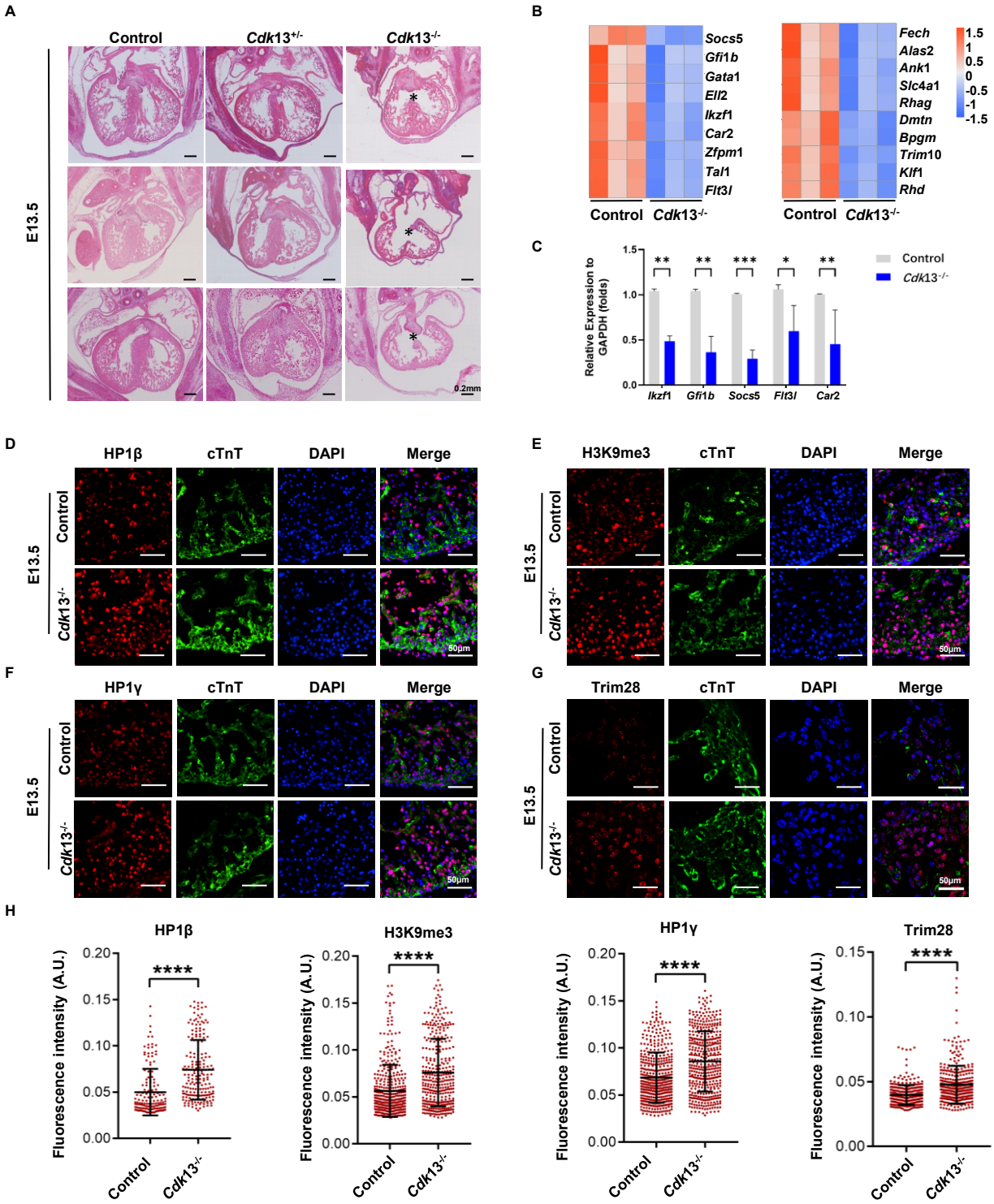
A
Control
Cdk13+/-
Cdk13-/-
E13.5
0.2mm
B
Socs5
Gfi1b
Gata1
Ell2
Ikzf1
Car2
Zfpm1
Tal1
Flt3l
Fech
Alas2
Ank1
Slc4a1
Rhag
Dmtn
Bpgm
Trim10
Klf1
Rhd
1.5
1
0.5
0
-0.5
-1
-1.5
Control
Cdk13-/-
C
Relative Expression to GAPDH (folds)
Ikzf1
Gfi1b
Socs5
Flt3l
Car2
D
HP1β
cTnT
DAPI
Merge
50μm
E
H3K9me3
F
HP1γ
G
Trim28
H
Fluorescence intensity (A.U.)
****

835 **Fig. 2 |Deletion of *Cdk*13 in mice causes embryonic morphology defects and increased**
836 **H3K9me3-heterochromatinization in cardiomyocytes.**
837 **A**, *Cdk*13$^{-/-}$ resulted in abnormal cardiac structure such as lack of interventricular septum in
838 mouse E13.5 embryos. The embryos were stained with haematoxylin and eosin. The left panel
839 shows the control hearts, the middle panel shows *Cdk*13$^{+/-}$ embryo hearts, and the right panel
840 shows *Cdk*13$^{-/-}$ embryo hearts. Asterisks indicate the area with ventricular septal defects. **B**, The
841 heatmap shows downregulated genes related to development (left) and myeloid cells (right). **C**,
842 qRT-PCR confirmed the reduced transcription level of randomly selected genes from (d) in
843 *Cdk*13$^{-/-}$ E13.5 heart tissue. The data are presented as the means ± SEMs. *$P < 0.05$, **$P<0.01$,
844 ***$P < 0.001$, t-test. **D-G**, Increased heterochromatinization in E13.5 *Cdk*13$^{-/-}$ embryonic heart
845 cells. Immunofluorescence staining was performed using antibodies against known markers of
846 heterochromatin, including HP1β (**D**), H3K9me3 (**E**), HP1γ (**F**), and Trim28 (**G**), which are
847 labelled in red. cTnT-labelled cardiomyocytes are shown in green, and DAPI is shown in blue.
848 All images show the left ventricle position. The scale bar was 50 μm. **H**, The fluorescence
849 intensity of single cells is shown according to the immunofluorescence staining results (**D-G**).
850 Each point represents a cell, and more than 300 cells per condition were analyzed. A. U, arbitrary
851 unit, $n = 3$, t-test. ****$P < 0.0001$.
852
853

Fig. 3

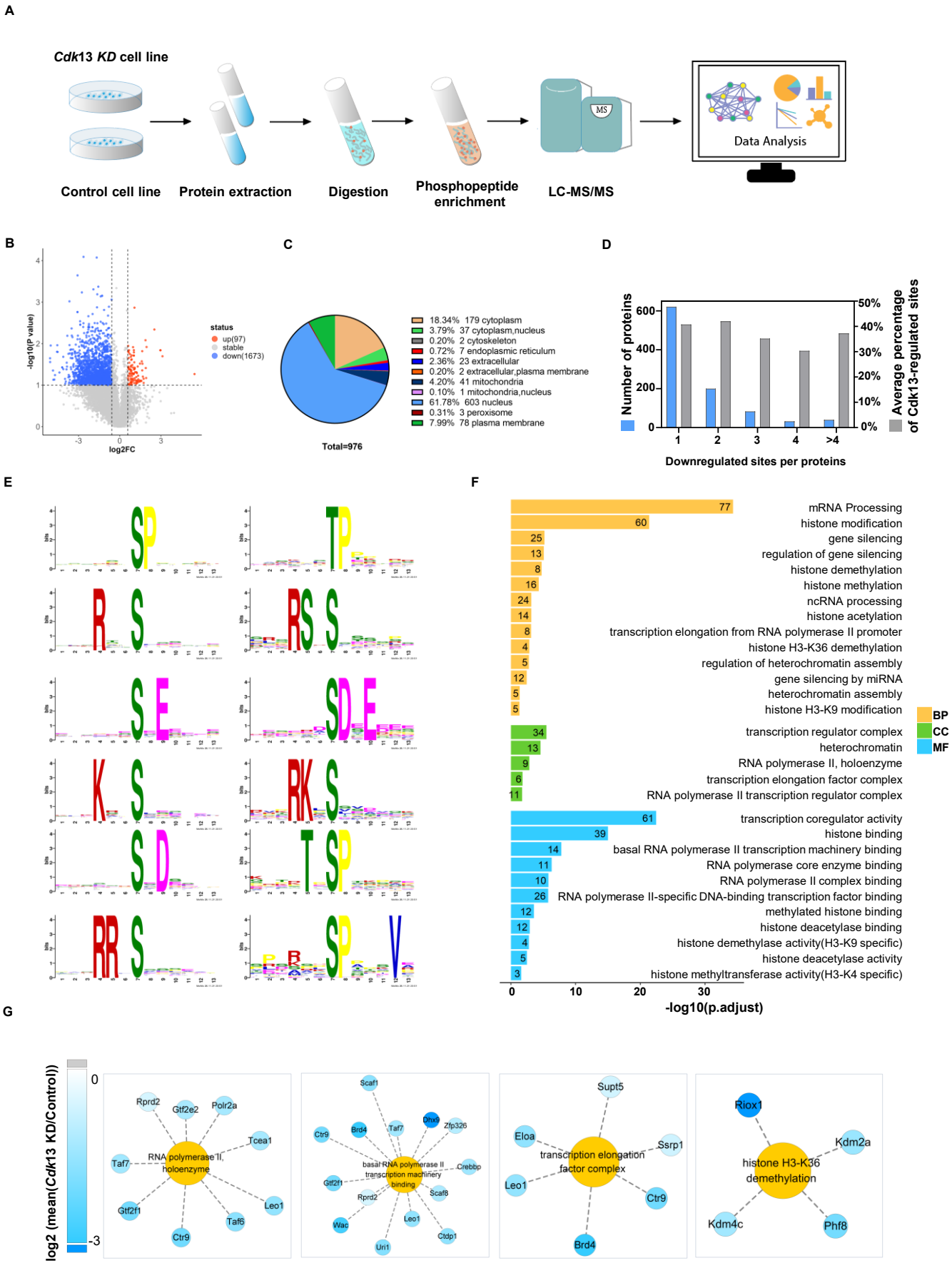
A
Cdk13 KD cell line
Control cell line
Protein extraction
Digestion
Phosphopeptide enrichment
LC-MS/MS
MS
Data Analysis
B
-log10(P value)
log2FC
status
up(97)
stable
down(1673)
C
18.34% 179 cytoplasm
3.79% 37 cytoplasm,nucleus
0.20% 2 cytoskeleton
0.72% 7 endoplasmic reticulum
2.36% 23 extracellular
0.20% 2 extracellular,plasma membrane
4.20% 41 mitochondria
0.10% 1 mitochondria,nucleus
61.78% 603 nucleus
0.31% 3 peroxisome
7.99% 78 plasma membrane
Total=976
D
Number of proteins
Average percentage of Cdk13-regulated sites
Downregulated sites per proteins
E
F
mRNA Processing
histone modification
gene silencing
regulation of gene silencing
histone demethylation
histone methylation
ncRNA processing
histone acetylation
transcription elongation from RNA polymerase II promoter
histone H3-K36 demethylation
regulation of heterochromatin assembly
gene silencing by miRNA
heterochromatin assembly
histone H3-K9 modification
transcription regulator complex
heterochromatin
RNA polymerase II, holoenzyme
transcription elongation factor complex
RNA polymerase II transcription regulator complex
transcription coregulator activity
histone binding
basal RNA polymerase II transcription machinery binding
RNA polymerase core enzyme binding
RNA polymerase II complex binding
RNA polymerase II-specific DNA-binding transcription factor binding
methylated histone binding
histone deacetylase binding
histone demethylase activity(H3-K9 specific)
histone deacetylase activity
histone methyltransferase activity(H3-K4 specific)
BP
CC
MF
-log10(p.adjust)
G
log2 (mean(Cdk13 KD/Control))
RNA polymerase II, holoenzyme
basal RNA polymerase II transcription machinery binding
transcription elongation factor complex
histone H3-K36 demethylation

854 **Fig. 3 | Phosphoproteomic analysis of the global protein network targeted by Cdk13.**
855 **A**, Global phosphoproteomics workflow. **B**, Majority changes in protein phosphorylation are
856 downregulated. The volcano plot shows the detected S/T/Y sites in phosphorylation data. The X-
857 axis represents log2(fold change), while the Y-axis represents -log10(P values). Red indicates
858 upregulated sites, Blue indicates downregulated sites, and dotted lines represents the threshold of
859 fold change (1.5) and P value (0.1). Each point represents a S/T/Y site. **C**, The pie plot shows the
860 locations of downregulated proteins (fold change>1.5 and P < 0.1), most of these proteins
861 enriched in the nucleus. **D**, More than 30% protein phosphorylation sites are downregulated in
862 each group. The bar plot shows the relationship between the number of proteins (blue, left y-axis)
863 with downregulated protein phosphorylation sites, the percentage of downregulated sites (grey,
864 right y-axis), and the number of downregulated protein phosphorylation sites in each protein (x-
865 axis). **E**, The amino acid sequence logo illustrates the sequence preference around downregulated
866 phosphorylation sites after *Cdk*13 KD. The motifs were centered on the downregulation sites and
867 extended 6 positions upstream and downstream from 1639 unique peptide sequences. **F**, Gene
868 Ontology enrichment analysis of proteins with reduced phosphorylation after *Cdk*13 KD.
869 Selected terms for each group in the BP, CC and MF categories are shown. Yellow represents
870 biological process (BP); green represents cellular component (CC); blue represents molecular
871 function (MF). The x-axis represents the -log10 (adjusted *P* value), and the numbers on the color
872 bars indicate the numbers of genes enriched for each term. **G**, Proteins with loss of
873 phosphorylation are associated with RNA polymerase II initiation and elongation, as well as
874 regulators of specific histone modifications.
875
876

Fig. 4

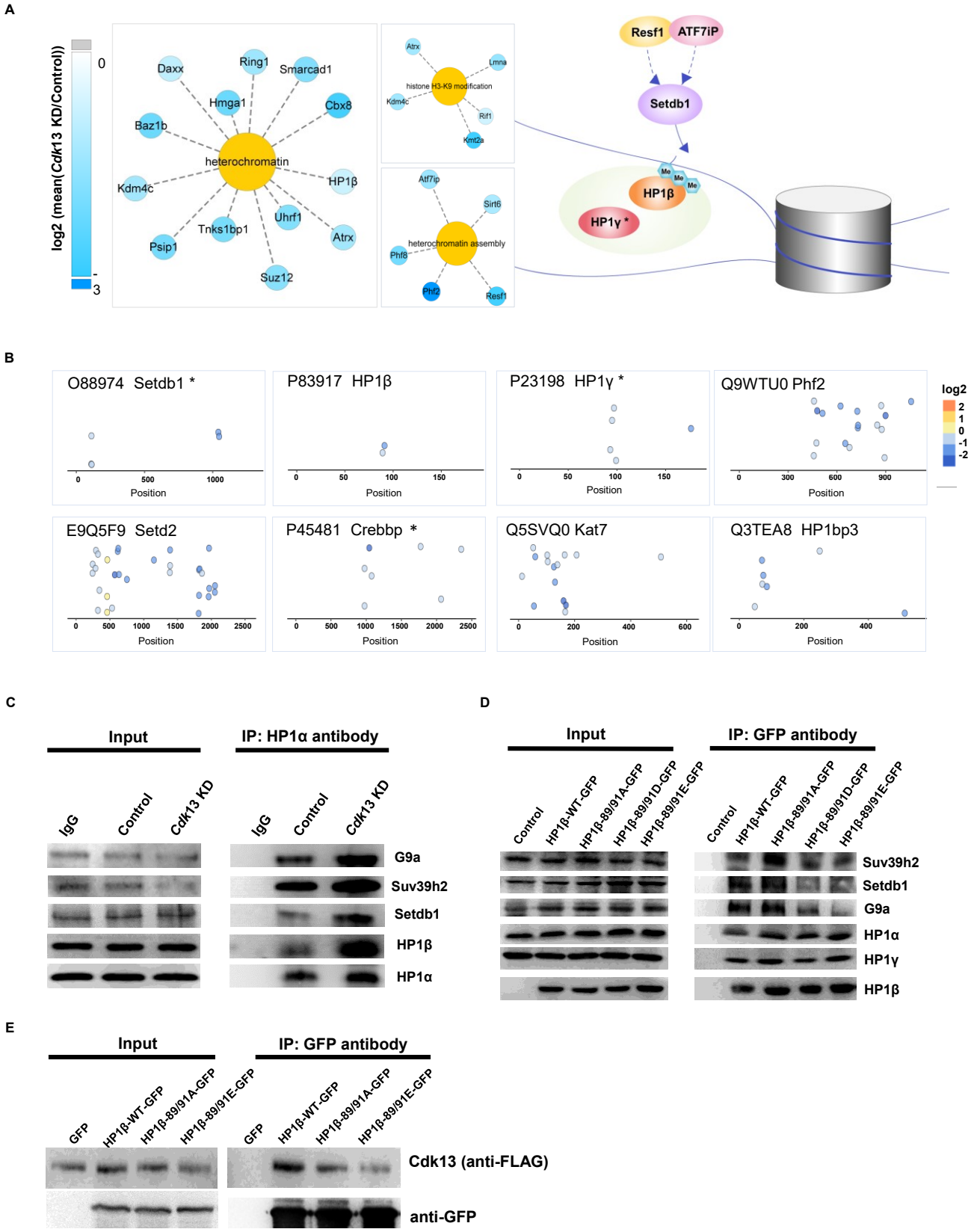
A
log2 (mean(Cdk13 KD/Control))
0
-3
Daxx
Ring1
Smarcad1
Hmga1
Cbx8
Baz1b
heterochromatin
HP1β
Kdm4c
Tnks1bp1
Uhrf1
Atrx
Psip1
Suz12
Atrx
Lmna
histone H3-K9 modification
Kdm4c
Rif1
Kmt2a
Atf7ip
Sirt6
heterochromatin assembly
Phf8
Phf2
Resf1
Resf1
ATF7iP
Setdb1
Me
HP1β
HP1γ *
B
O88974 Setdb1 *
P83917 HP1β
P23198 HP1γ *
Q9WTU0 Phf2
log2
2
1
0
-1
-2
Position
E9Q5F9 Setd2
P45481 Crebbp *
Q5SVQ0 Kat7
Q3TEA8 HP1bp3
C
Input
IP: HP1α antibody
IgG
Control
Cdk13 KD
G9a
Suv39h2
Setdb1
HP1β
HP1α
D
Input
IP: GFP antibody
Control
HP1β-WT-GFP
HP1β-89/91A-GFP
HP1β-89/91D-GFP
HP1β-89/91E-GFP
Suv39h2
Setdb1
G9a
HP1α
HP1γ
HP1β
E
Input
IP: GFP antibody
GFP
HP1β-WT-GFP
HP1β-89/91A-GFP
HP1β-89/91E-GFP
Cdk13 (anti-FLAG)
anti-GFP

877 **Fig. 4 | Inhibition of heterochromatin complex formation by specific phosphorylation of**
878 **HP1β.**
879 **A**, Heterochromatin proteins with loss of phosphorylation and a possible model of
880 heterochromatin assembly according to the results of global phosphoproteomics. **B**, The dot plot
881 shows the change in representative protein phosphorylation sites; each point represents an amino
882 acid (S/T) as a substrate for phosphorylation. The X-axis indicates the location of the
883 phosphorylation site within the protein. The names of the selected proteins, including
884 heterochromatin proteins H3K9me3 HMT- Setdb1 and HP1β, are indicated, and Log2 values
885 indicate the site-specific phosphorylation ratio of *Cdk*13 KD/Control. **C**, Coimmunoprecipitation
886 with an HP1α antibody followed by Western blot analysis was done to analyse the interactions of
887 HP1α with G9a, Suv39h2, Setdb1, and HP1β in mouse embryonic fibroblasts (MEFs) infected
888 with lentiviruses bearing shRNA in control or *Cdk*13 KD group. **D**, Phosphorylation at Ser89/91
889 of HP1β inhibited the binding of HP1β to the H3K9-associated methyltransferases, G9a,
890 Suv39h2, and Setdb1. **E**, Co-immunoprecipitation revealed an interaction between Cdk13 and
891 HP1β, which was inhibited by HP1β phosphorylation. The anti-Flag antibody was used to
892 monitor the presence of Cdk13, and the anti-GFP antibody was used to immunoprecipitate the
893 GFP-tagged wild type or mutant of HP1β.
894
895

Fig. 5

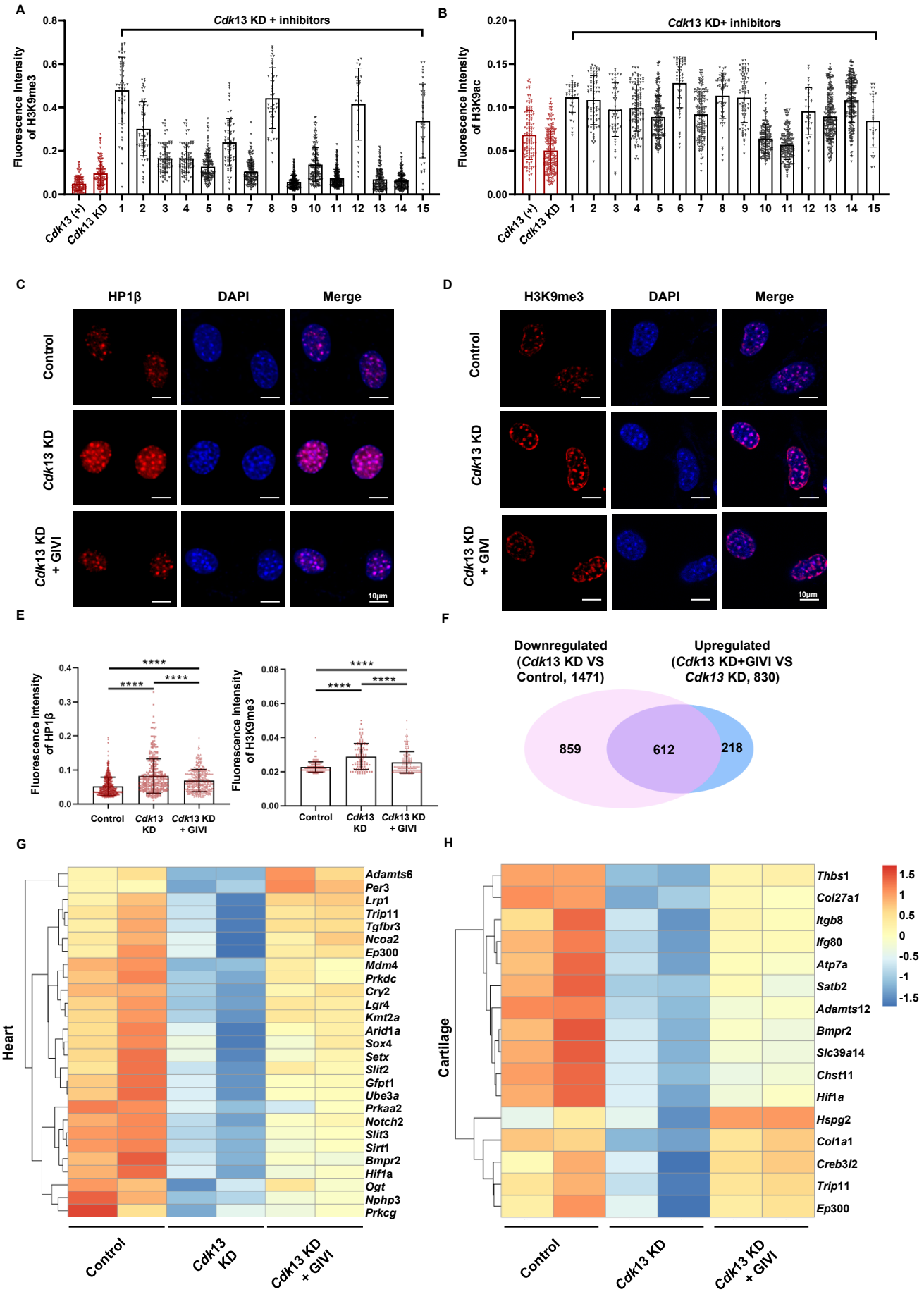
A
Cdk13 KD + inhibitors
Fluorescence Intensity of H3K9me3
Cdk13 (+)
Cdk13 KD
B
Cdk13 KD+ inhibitors
Fluorescence Intensity of H3K9ac
C
HP1β
DAPI
Merge
Control
Cdk13 KD
Cdk13 KD + GIVI
10μm
D
H3K9me3
DAPI
Merge
E
Fluorescence Intensity of HP1β
Fluorescence Intensity of H3K9me3
Control
Cdk13 KD
Cdk13 KD + GIVI
F
Downregulated (Cdk13 KD VS Control, 1471)
Upregulated (Cdk13 KD+GIVI VS Cdk13 KD, 830)
859
612
218
G
Heart
Adamts6
Per3
Lrp1
Trip11
Tgfbr3
Ncoa2
Ep300
Mdm4
Prkdc
Cry2
Lgr4
Kmt2a
Arid1a
Sox4
Setx
Slit2
Gfpt1
Ube3a
Prkaa2
Notch2
Slit3
Sirt1
Bmpr2
Hif1a
Ogt
Nphp3
Prkcg
H
Cartilage
Thbs1
Col27a1
Itgb8
Ifg80
Atp7a
Satb2
Adamts12
Bmpr2
Slc39a14
Chst11
Hif1a
Hspg2
Col1a1
Creb3l2
Trip11
Ep300

896
897 **Fig. 5 | The depletion of *Cdk*13-induced heterochromatinization was antagonized by**
898 **H3K9me3 inhibitors.**
899 **A, B** Fifteen small molecule inhibitors were screened by immunofluorescence staining assay to
900 inhibit H3K9me3 and increase H3K9ac in *Cdk*13 KD cells. The left panel shows the
901 quantification of fluorescence intensity of H3K9me3, and the right panel shows the
902 quantification of H3K9ac fluorescence intensity. Each point represents a cell, and 30-250 cells
903 per condition were analyzed. The data are presented as means ± SEMs.
904 **C**, **D**, The small molecule drug givinostat (GIVI) (2.5 nM) blocked heterochromatin formation
905 caused by *Cdk*13 knockdown. The representative immunofluorescence staining for HP1β (**C**) and
906 H3K9me3 (**D**) in MEFs is shown. **E**, The quantification of the relative intensity of HP1β and
907 H3K9me3 is shown. Each point represents a cell, and more than 300 cells per condition were
908 analyzed. The data are presented as the means ± SEMs. ****$P < 0.0001$, t-test. **F**, The GIVI
909 treatment could efficiently recover more than 40% *Cdk*13 KD downregulated genes. The overlap
910 between downregulated genes in *Cdk*13-depleted MEFs and upregulated genes after treatment
911 with 2.5 nM GIVI is shown. **G**, **H**, RNA sequencing analysis of control, *Cdk*13 KD and *Cdk*13
912 KD +GIVI showed rescue trends. A heatmap shows several differentially expressed genes
913 (DEGs) related to heart function (**G**) and cartilage (**H**).
914
915

Fig. 6

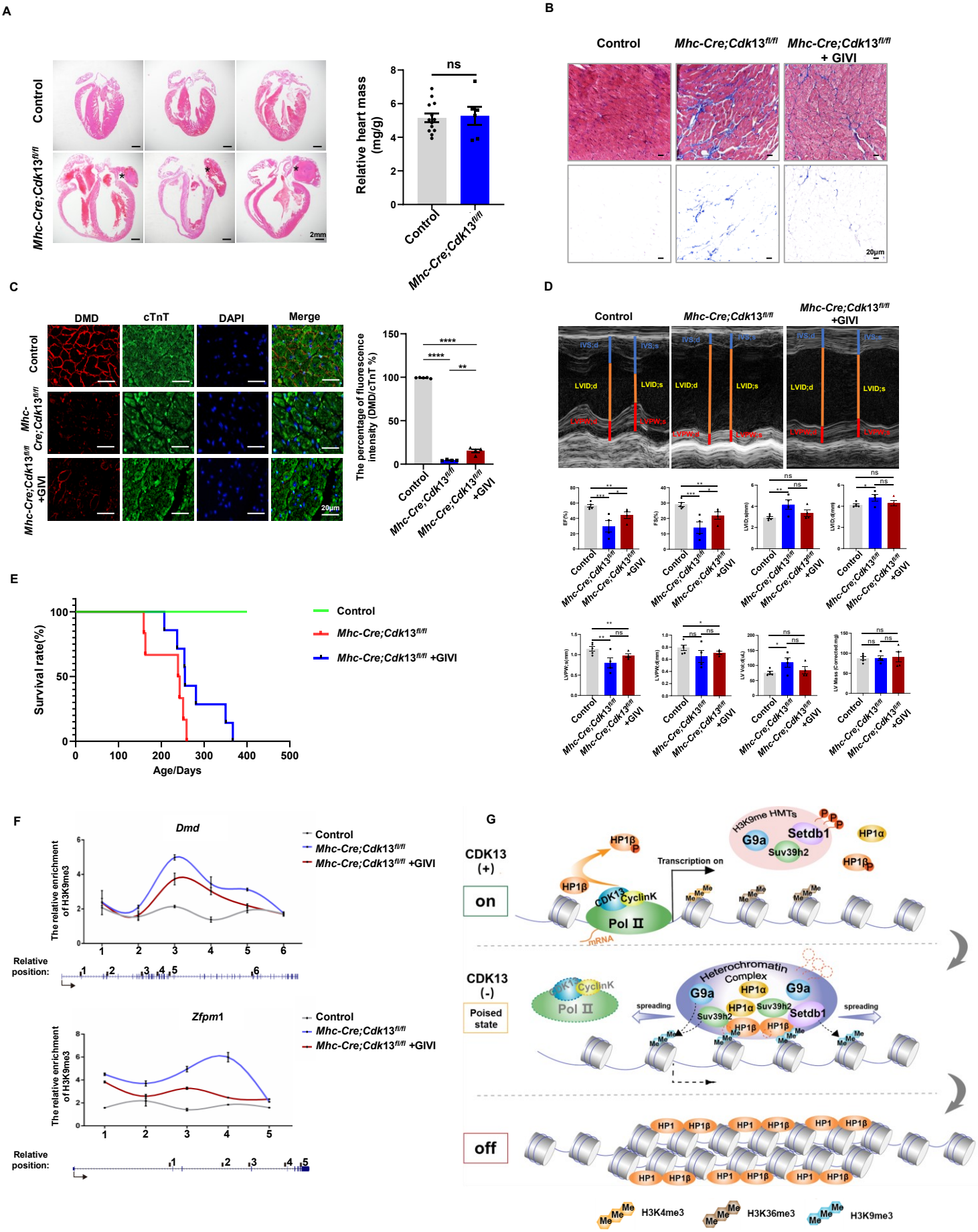
A
Control
Mhc-Cre;Cdk13fl/fl
2mm
Relative heart mass (mg/g)
ns
B
Control
Mhc-Cre;Cdk13fl/fl
Mhc-Cre;Cdk13fl/fl + GIVI
20μm
C
DMD
cTnT
DAPI
Merge
Control
Mhc-Cre;Cdk13fl/fl
Mhc-Cre;Cdk13fl/fl +GIVI
20μm
The percentage of fluorescence intensity (DMD/cTnT %)
D
Control
Mhc-Cre;Cdk13fl/fl
Mhc-Cre;Cdk13fl/fl +GIVI
IVS;d
IVS;s
LVID;d
LVID;s
LVPW;d
LVPW;s
E
Survival rate(%)
Age/Days
Control
Mhc-Cre;Cdk13fl/fl
Mhc-Cre;Cdk13fl/fl +GIVI
F
Dmd
Zfpm1
The relative enrichment of H3K9me3
Relative position:
G
CDK13 (+)
on
HP1β
CDK13
CyclinK
Pol Ⅱ
JnRNA
Transcription on
H3K9me HMTs
G9a
Setdb1
Suv39h2
HP1α
CDK13 (-)
Poised state
Heterochromatin Complex
spreading
off
HP1
H3K4me3
H3K36me3
H3K9me3

916
917 **Fig. 6 |Heart defects caused by *Cdk*13 deletion in mice are alleviated by GIVI.**
918 **A**, Ventricular lumen enlargement and ventricular wall thinning were observed in 8-month-old
919 *Mhc-cre;Cdk*13$^{fl/fl}$ mice. Haematoxylin and eosin were used to illustrate the heart structure.
920 Asterisks indicate atrial congestion. The right panel shows the statistics of the heart weight (mg)
921 relative to body weight (g). **B**, GIVI partially reversed fibrosis caused by *Cdk*13 knockout. The
922 hearts of mice stained with Masson's stain to indicate the pathological fibrosis process. The scale
923 bar was 50 μm. **C**, GIVI or DMSO treated heart tissues were stained with antibodies against
924 Dmd (red) and cTnT (green). The right panel shows the percentage Dmd and TnT-positive cells
925 by fluorescence intensity analysis, $n = 4$. $^{**}P < 0.01$, $^{****}P < 0.0001$, t-test. **D**, echocardiographic
926 tracing of mouse hearts. IVS indicates interventricular septum. LVID indicates left ventricular
927 internal diameter. LVPW indicates left ventricular posterior wall. EF indicates ejection fraction;
928 FS indicates fractional shortening; LVPW indicates left ventricular posterior wall, systolic (s);
929 LVPW indicates left ventricular posterior wall, diastolic(d); LV mass indicates left ventricular
930 mass. **E**, The survival rate of GIVI-treated *Mhc-cre*;*Cdk*13$^{fl/fl}$ mice was significantly increased
931 compared to the *Mhc-cre*;*Cdk13*$^{fl/fl}$ group without GIVI treatment. **F**, ChIP-qPCR analysis
932 showed that the enrichment of H3K9me3 in *Cdk*13 knockout embryos was decreased in the
933 presence of GIVI. The E17.5 heart tissue of control (*Cdk*13$^{fl/fl}$), *Cdk*13-deletion mutants (*Mhc-*
934 *cre;Cdk*13$^{fl/fl}$), and the GIVI-treated *Mhc-cre*;*Cdk*13$^{fl/fl}$ mice were collected to perform the ChIP
935 experiment, followed by qPCR analysis. The primers were designed to amplify the defined
936 regions in the *Dmd*, and *Zfpm*1 genes. **G**, Graphic model of Cdk13 in gene transcription and
937 heterochromatin formation. The Top panel shows Cdk13 maintains normal transcription
938 activation by phosphorylating heterochromatin proteins. The middle panel shows that the
939 deletion of *Cdk*13 causes a loss of HP1β phosphorylation, which increases the interaction
940 between HP1β and heterochromatin proteins, leading to the spreading of poised heterochromatin
941 structure at the euchromatic gene region. At the bottom, a stable repressive facultative
942 heterochromatin structure is formed, resulting in the subsequent gene silencing. ns, not
943 significant: $P > 0.05$; $^{*}P < 0.05$; $^{**}P < 0.01$; $^{***}P < 0.001$; $^{****}P < 0.0001$, t-test.
944
945
946
947
948
949
950
951
952
953
954
955

Supplementary Fig. 1

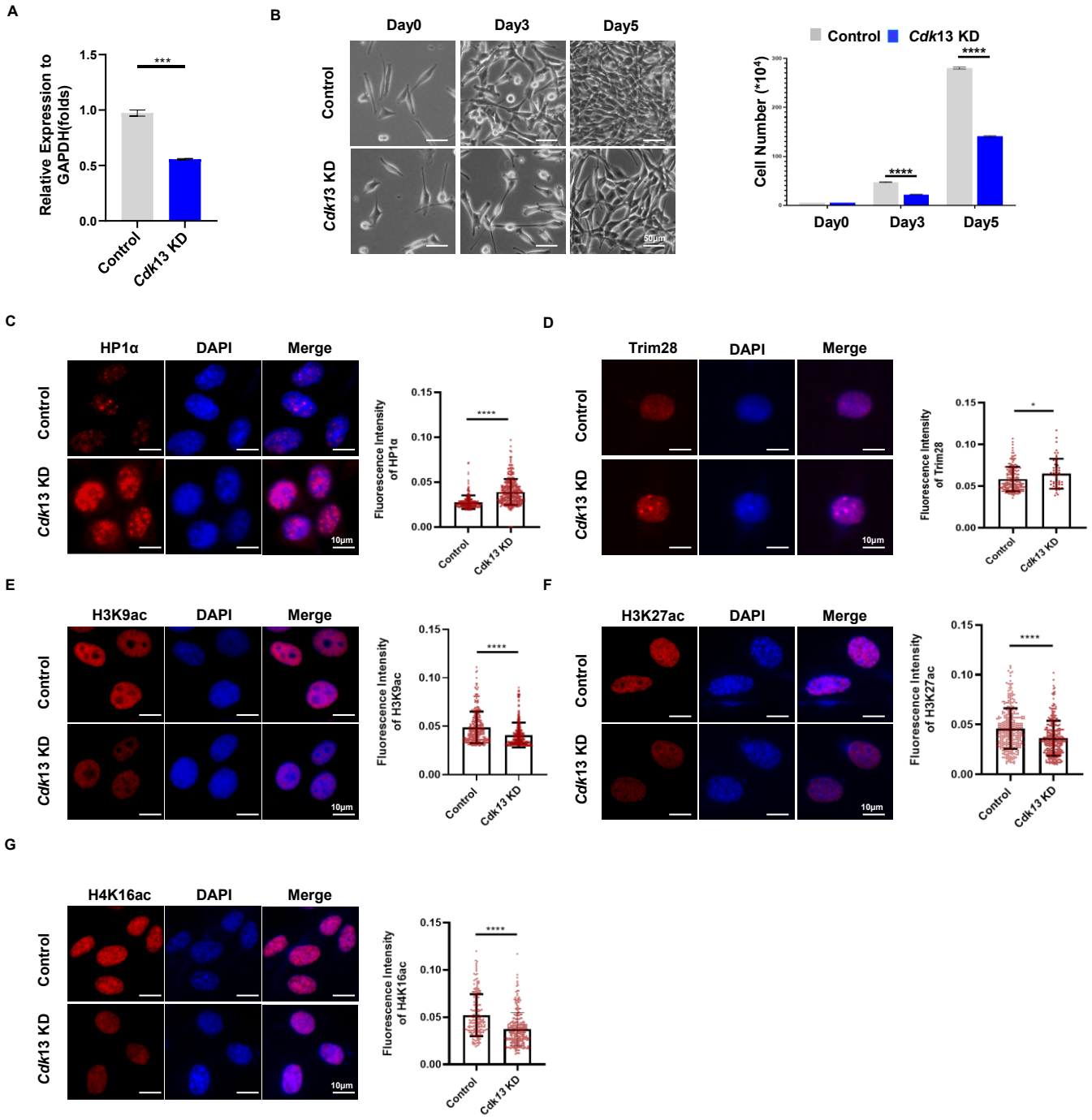

956 **Supplementary Fig. 1 | Depletion of *Cdk*13 inhibits cell proliferation and markers of active**
957 **chromatin**
958 **A**, *Cdk*13 was efficiently knockdown (KD) by shRNA in MEFs. RT-qPCR was performed to
959 examine the expression of *Cdk*13. The data are presented as the means ± SEMs. ***$P < 0.001$. t-
960 test. **B**, *Cdk*13 KD compromised cell proliferation. The images of cells on day 0, day 3, and day
961 5 (left panel), and the quantification of cell numbers (right panel) are shown. The data are
962 presented as the means ± SEMs. ****$P < 0.0001$, t-test. **C-G**, The left panel shows
963 representative immunofluorescence staining for HP1α (c), Trim28 (d), H3K9ac (e), H3K27ac (f),
964 and H4K16ac (g) in control and *Cdk*13 KD mouse embryonic fibroblasts (MEFs) with lentivirus
965 shRNA. The right panel shows the quantification of fluorescence intensity of the corresponding
966 images. Each point represents a cell, and more than 300 cells per condition were analyzed. The
967 data are presented as the means ± SEMs. *$P < 0.05$, ****$P < 0.0001$, t-test.
968
969

Supplementary Fig. 2

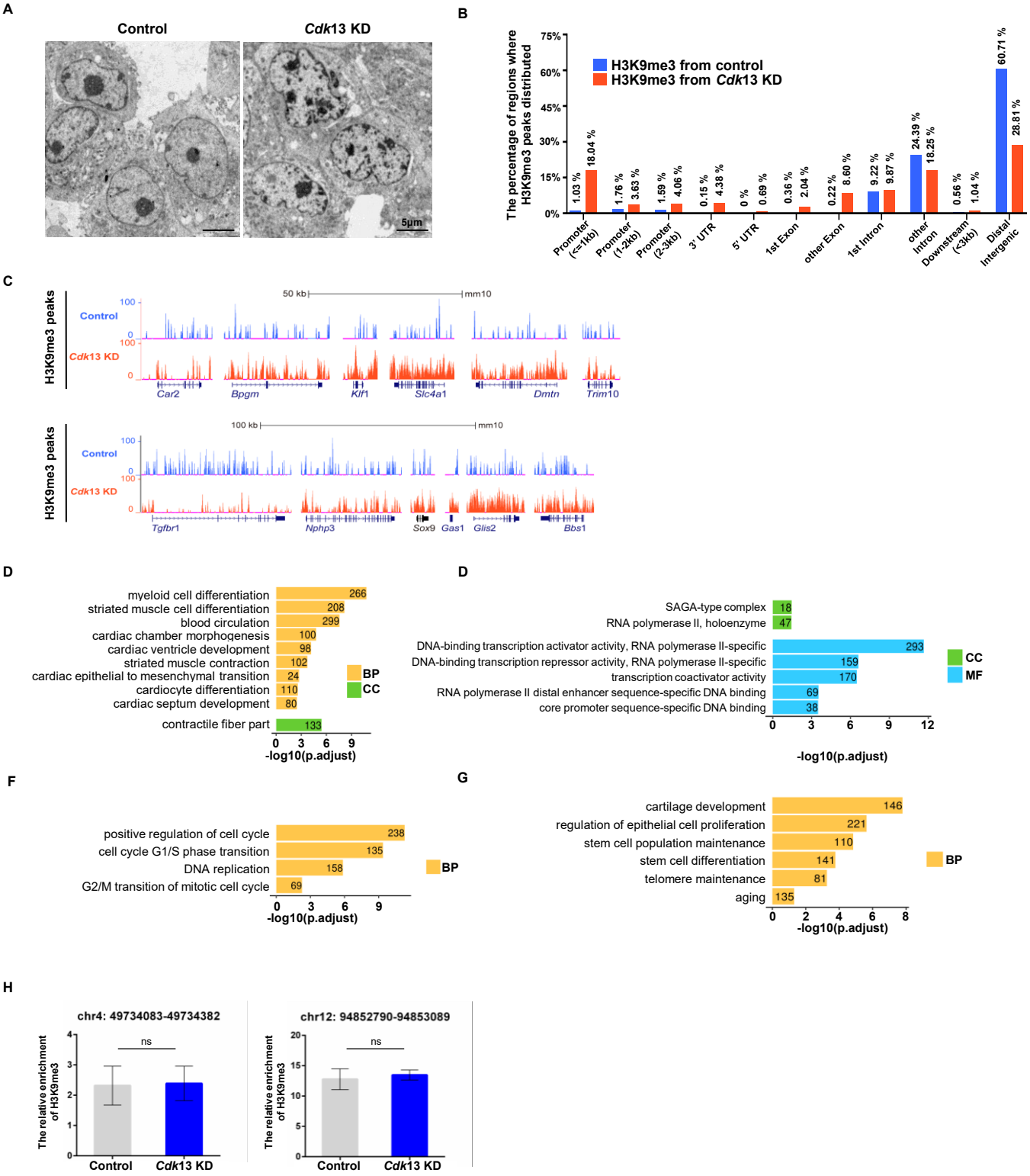

970 **Supplementary Fig. 2 | Depletion of *Cdk*13 promotes H3Kme3-heterochromatin spreading.**
971 **A**, Representative transmission electron microscopy images show heterochromatin in control and
972 MEFs with *Cdk*13 KD. n = 15 nuclei. **B**, The relative percentage of H3K9me3 in the promoter
973 region, exon region, 3' UTR and distal intergenic regions of control and *Cdk*13 KD MEFs. The
974 bar plot shows the H3K9me3 peak percentage of each region. The blue bar represents the control
975 group, and the red bar represents the *Cdk*13 KD group. **C**, The representative genes show the
976 distribution of H3K9me3 peaks. The views of H3K9me3 in the UCSC genome is shown. The
977 blue represents the control group, and the red represents the *Cdk*13 KD group. **D-G**, Selected
978 Gene Ontology (GO) terms enriched with H3K9me3 in the promoter after *Cdk*13 KD. The
979 column in yellow, green and blue represents genes involved in biological process (BP), cellular
980 component (CC), and molecular function (MF). The x-axis represents the -log10 (adjusted P
981 value), and the numbers on the bars are the numbers of genes enriched for each term. **H**, ChIP-
982 qPCR results verified the intergenic region where H3K9me3 showed no difference.
983
984

Supplementary Fig. 3

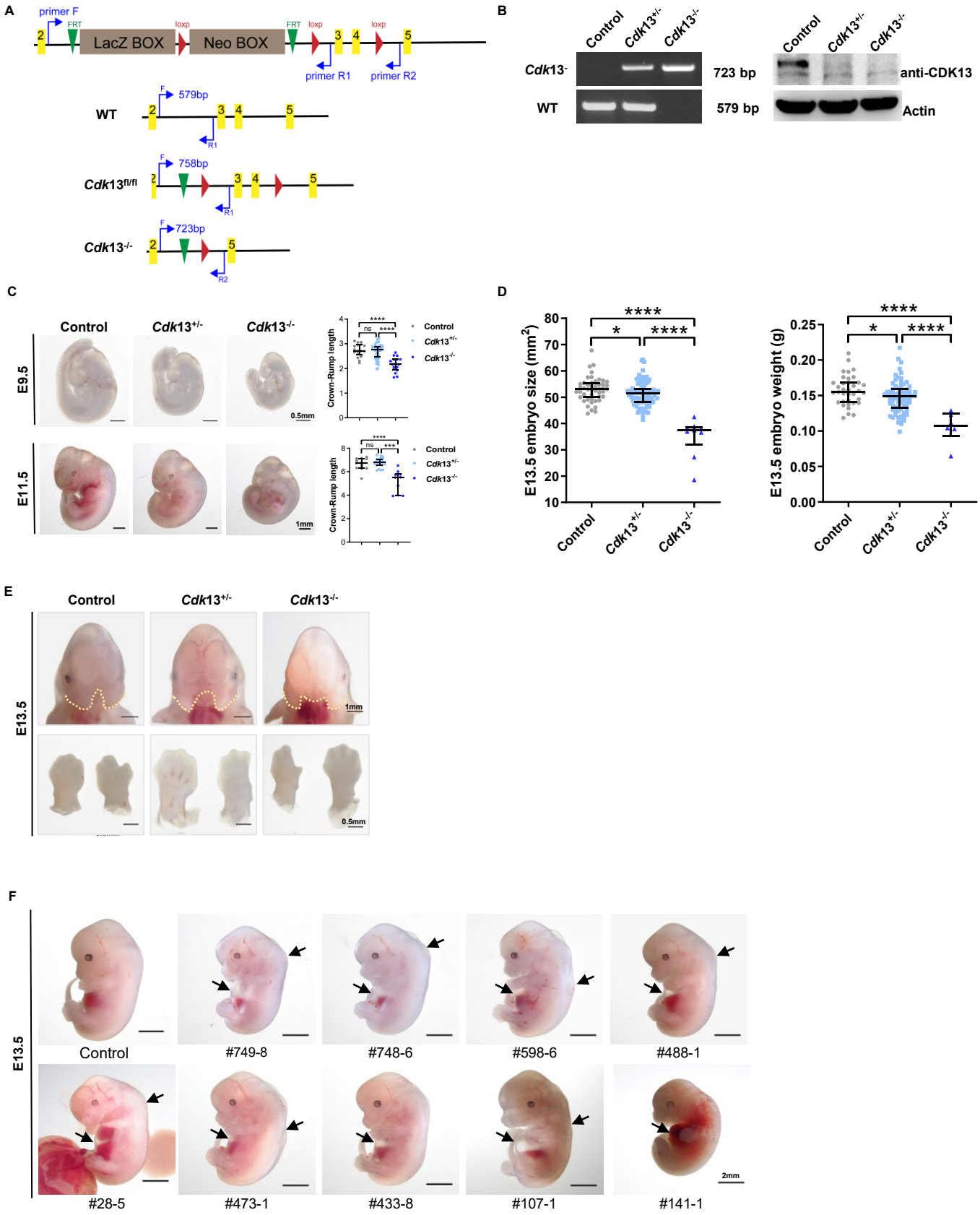

985 **Supplementary Fig. 3 | *Cdk*13 knockout in mice causes embryonic morphology defects.**
986 **A**, Schematic illustration of the constructs used to generate *Cdk*13 knockout (*Cdk*13$^{-/-}$) mice and
987 PCR primers monitoring the deletion efficiency of *Cdk*13$^{-/-}$mice. **B**, The deletion efficiency of
988 *Cdk*13$^{-/-}$ was confirmed by PCR in the left panel and Western blot analysis in the right panel.
989 E13.5 embryo tail tissue DNA was used for PCR. E13.5 mouse embryonic brain tissue was used
990 in the Western blotting to detect Cdk13 protein expression. Actin was used as an internal control.
991 **C**, *Cdk*13 knockout (*Cdk*13$^{-/-}$) resulted in smaller size embryos at E9.5 and E11.5 than controls.
992 The right panel shows the quantification of the Crown-Rump length of E9.5 and E11.5 embryos.
993 The number of embryos at E9.5 was Control, n=17; *Cdk*13$^{+/-}$, n=44; *Cdk*13$^{-/-}$, n=17. The number
994 of embryos at E11.5 was control, n=13; *Cdk*13$^{+/-}$, n=24; *Cdk*13$^{-/-}$, n=10, with a scale bar of
995 0.5mm. The data are presented as the means ± SEMs. ***$P < 0.001$, ****$P < 0.0001$, t-test. **D**
996 Quantification of the size and weight of E13.5 embryos. The number of embryos: control, n=36;
997 *Cdk*13$^{+/-}$, n=74; *Cdk*13$^{-/-}$, n=6. **E**, *Cdk*13$^{-/-}$ resulted in craniofacial defects (upper panel) and
998 digital anomalies (lower panel) in mouse E13.5 embryos. The scale bar was 0.5mm for digital
999 anomalies and 1mm for craniofacial defects. **F**, *Cdk*13 knockout resulted in pleural/back effusion
1000 and smaller size of mouse embryos at E13.5. The unique code number of each fetus is also
1001 indicated.
1002
1003

Supplementary Fig. 4

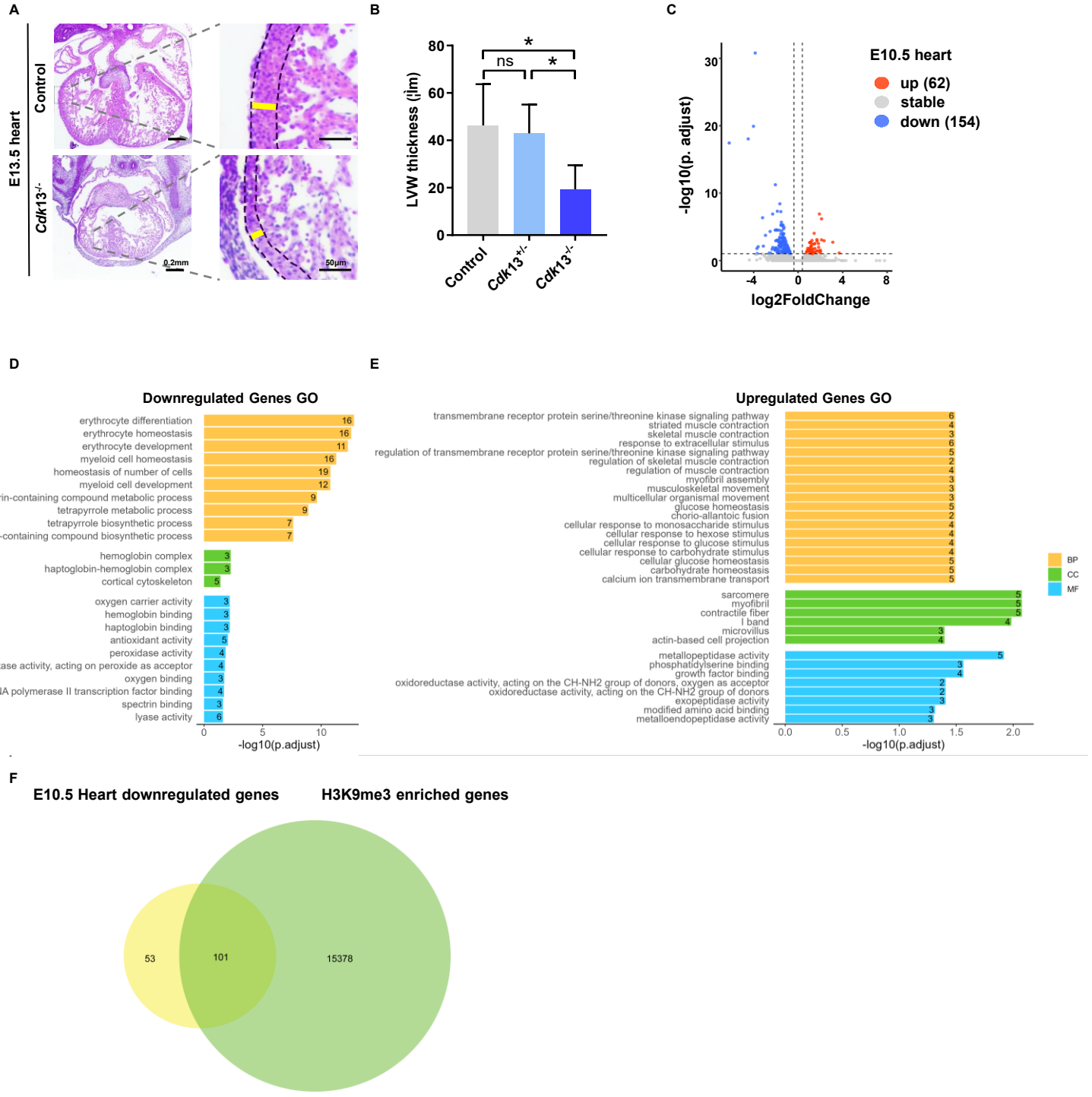

1004 **Supplementary Fig. 4 | *Cdk*13 deletion causes embryo heart defects and downregulation of**
1005 **genes. A**, *Cdk*13 knockout resulted in a defective interventricular septum and decreased
1006 thickness of the ventricular walls in E13.5 embryos. The scale bar was 200μm (left) and 50μm
1007 (right). **B**, Quantification of the thickness of the ventricular wall using E13.5 *Cdk*13$^{-/-}$ mutant and
1008 control heart tissues. The data are presented as means ± SEMs. N=3, *$P < 0.05$, t-test. **C**, The
1009 volcano plot of RNA sequencing data shows differentially expressed genes (DEGs; fold
1010 change>1.3 and adjusted $P < 0.1$) in E10.5 heart. The number of downregulated genes is 2.5
1011 folds of the number of upregulated genes. The red points represent upregulated genes, and the
1012 blue points represent downregulated genes; the dotted line indicates the threshold of the fold
1013 change and adjusted P value. **D**, **E**, Gene Ontology analysis of the altered expression of genes
1014 from RNA-seq. **F**, Two-thirds of downregulated genes in E10.5 hearts from RNA-seq
1015 overlapped with the corresponding genes showing increased H3K9me3 in *Cdk*13 KD MEFs (Fig.
1016 1c).
1017
1018

Supplementary Fig. 5

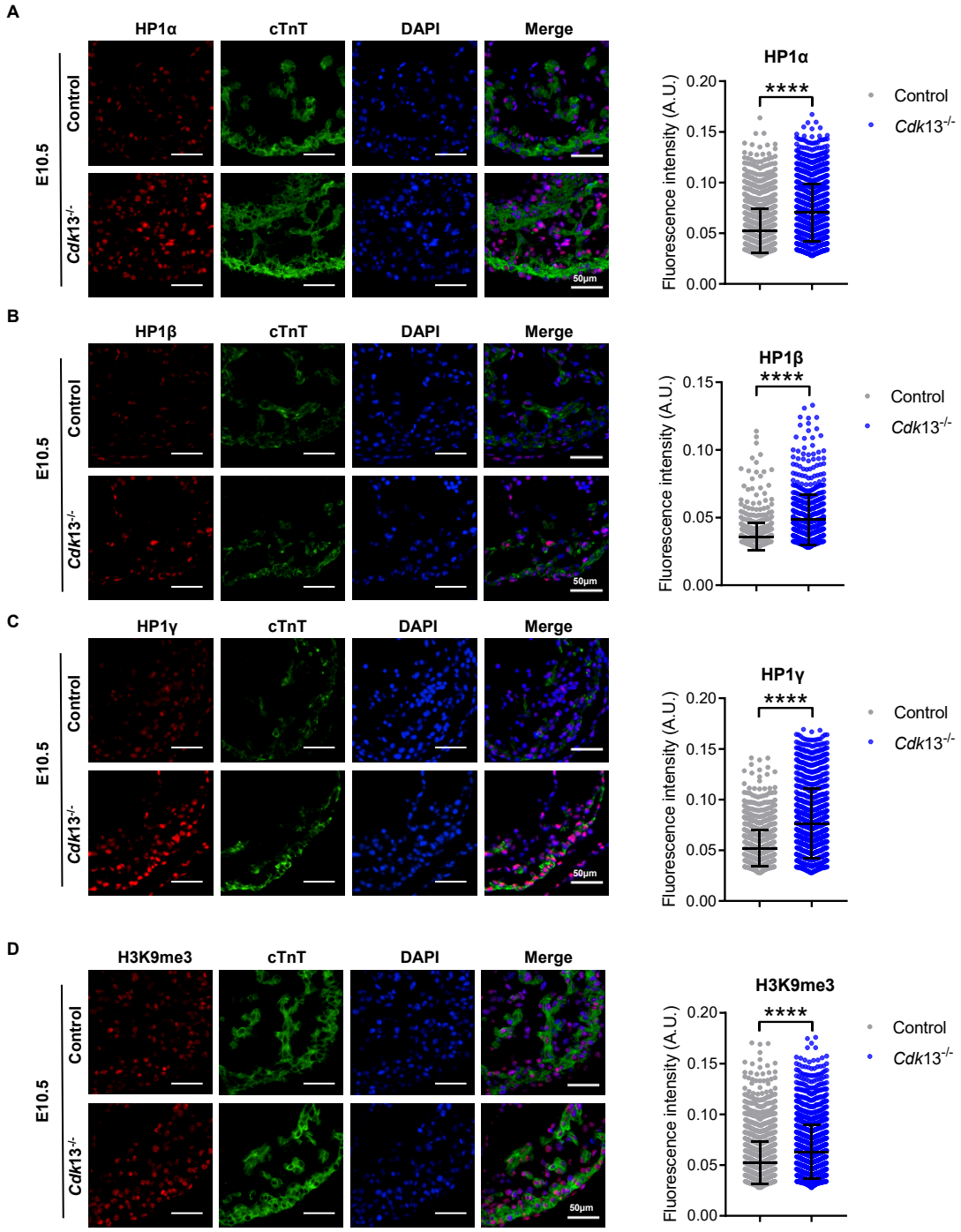

1019 **Supplementary Fig. 5 | *Cdk*13 deletion increases heterochromatinization in E10.5 mouse**
1020 **embryonic heart tissues.** The left panel shows immunofluorescence staining performed using
1021 antibodies against markers of heterochromatin, HP1α (**A**), HP1β (**B**), HP1γ (**C**), and H3K9me3
1022 (**D**), which are labeled in red. Cardiomyocytes labeled with cTnT are green, and DAPI is shown
1023 in blue. All images show the left ventricle position. The scale bar was 50μm. The right panel
1024 shows the fluorescence intensity of single cell, and more than 200 cells per condition were
1025 analyzed (**A**-**D**). A. U, arbitrary unit, N = 3/4/5, t-test. ****P < 0.0001.
1026
1027

Supplementary Fig. 6

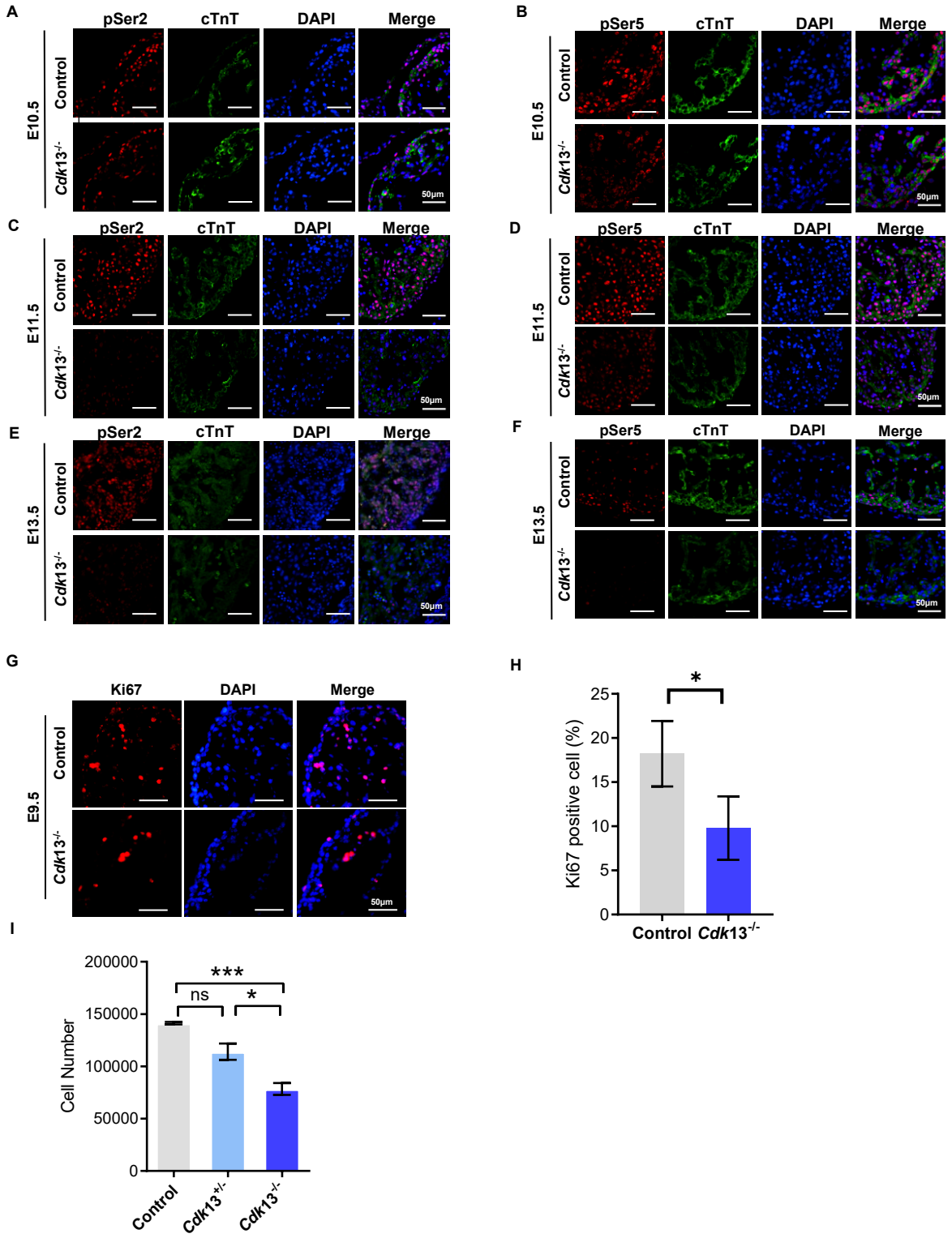

1028 **Supplementary Fig. 6 | *Cdk*13 deletion decreases phosphorylation of RNA polymerase II**
1029 **and cell proliferation. A-F**, Immunofluorescence staining was performed using antibodies
1030 against RNA polymerase II pSer2 (left) and pSer5 (right) in E10.5 (**A, B**), E11.5 (**C, D**) and
1031 E13.5 (**E, F**) embryonic heart tissues. All images show the left ventricle position. The scale bar
1032 was 50 μm. **G**, Immunofluorescence staining was performed using anti-Ki67 in E9.5 mouse
1033 embryonic heart tissues. The scale bar was 50 μm. **H**, Quantification of Ki67-positive cells. N=3
1034 *P <0.1, t-test (**I**) The total number of cells was decreased in E13.5 *Cdk*13$^{-/-}$ mouse embryos. The
1035 analyzed data are presented as means ± SEMs. N=3 *$P < 0.05$, ***$P < 0.001$, t-test.
1036
1037

Supplementary Fig. 7

A

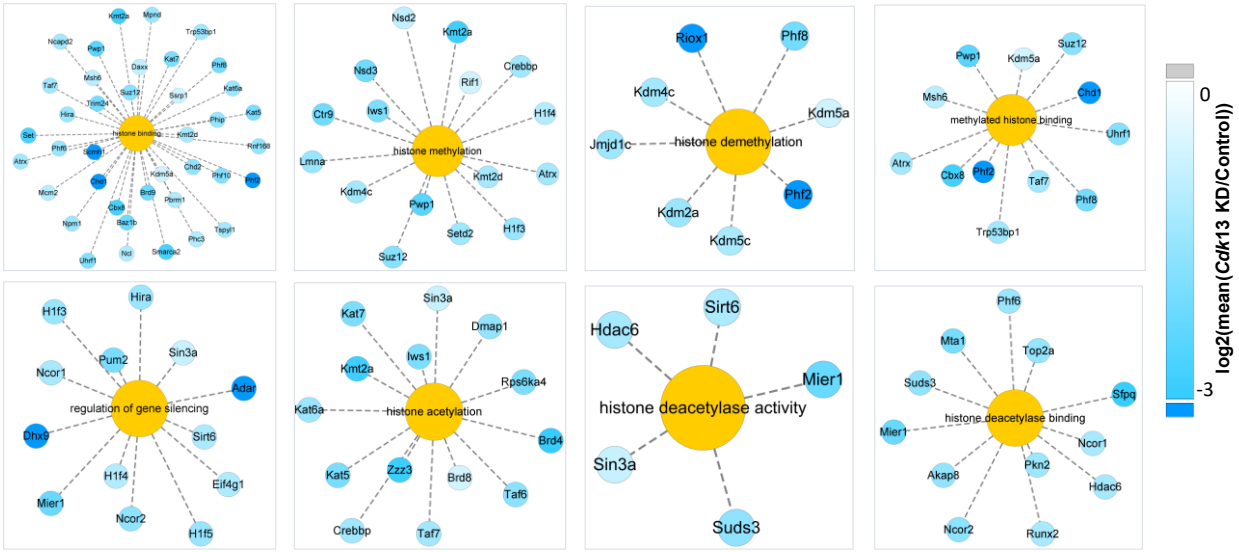

B

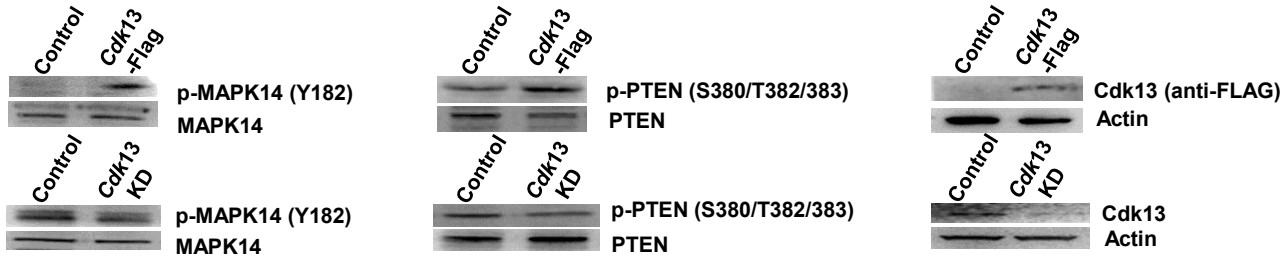

1038 **Supplementary Fig. 7 | Gene Ontology enrichment analysis and validation of Cdk13-**
1039 **dependent protein phosphorylation regulated by Cdk13.**
1040 **A**, simple network plot shows the selected Gene Ontology terms and related proteins with
1041 decreased phosphorylation upon *Cdk*13 KD, including histone binding, histone methylation and
1042 histone demethylation, histone acetylation and deacetylation. The colours of the protein nodes
1043 represent the log2 (mean fold change) values. **B**, The Western blotting analysis shows that the
1044 phosphorylations of MAPK14 and PTEN were regulated by Cdk13 in a dosage-dependent
1045 manner. The top panel shows the increased phosphorylation of p-MAPK14(Y182) and p-
1046 PTEN(S380/T382/383) in the presence of Cdk13 overexpression. The bottom panel shows the
1047 decreased phosphorylation of p-MAPK14(Y182) and p-PTEN(S380/T382/383) after depletion of
1048 *Cdk*13. The overexpression of Cdk13 was monitored using anti-FLAG antibody, and the Cdk13
1049 depletion efficiency was analyzed using the anti-CDK13 antibody.
1050
1051

Supplementary Fig. 8

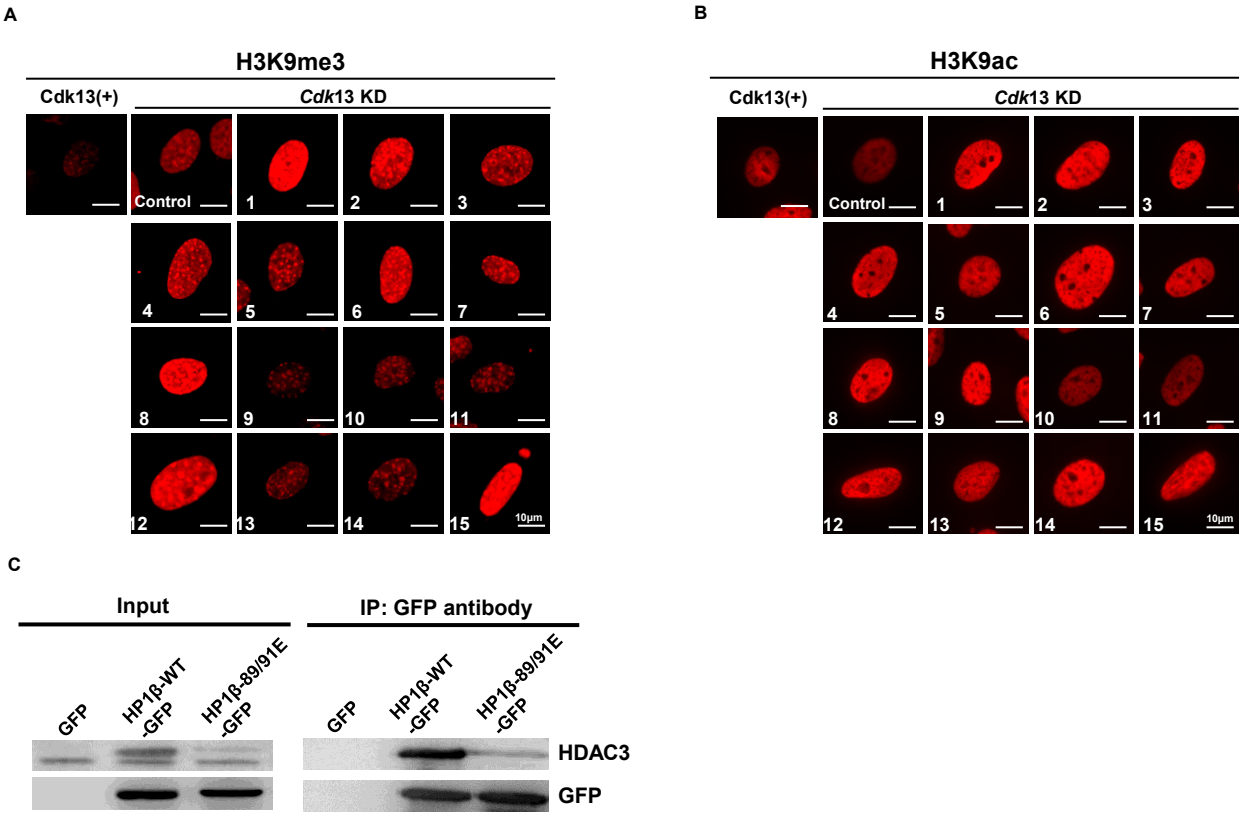

1052 **Supplementary Fig. 8 | A screen of small molecules antagonizing H3K9me3-**
1053 **heterochromatin**
1054 **A, B**, Representative immunofluorescence images for H3K9me3 and H3K9ac (red) in the
1055 presence of small molecules. **C**, IP experiments show the interaction between wild-type HP1β
1056 with HDAC3.
1057
1058

Supplementary Fig. 9

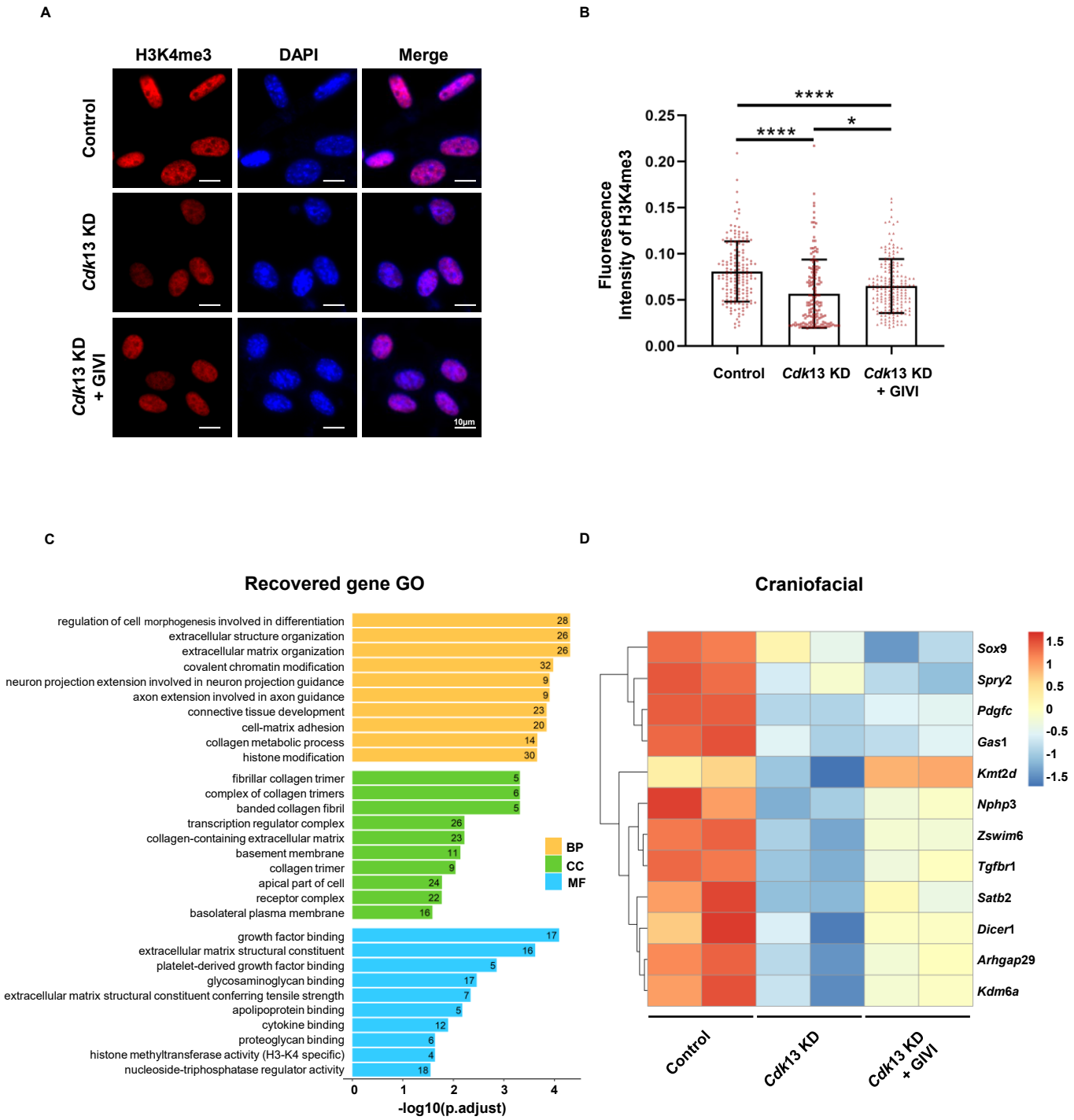

1059 **Supplementary Fig. 9 | GIVI prevents heterochromatinization to facilitate transcriptional**
1060 **activation.**
1061 **A**, GIVI partially recovers the intensity of H3K4me3 (red) caused by *Cdk*13 KD in MEFs. **B**,
1062 The quantification of H3K4me3 intensity is shown. Each point represents a cell, and more than
1063 300 cells were analysed under the same conditions. The data are presented as means ± SEMs.
1064 $*P < 0.05$, $****P < 0.0001$, t-test. **C**, Gene Ontology enrichment analysis of genes rescued by
1065 GIVI. Yellow, green and blue columns represent genes involved in biological process (BP),
1066 cellular component (CC) and molecular function (MF), respectively. **D**, A representative
1067 heatmap shows the RNA sequencing analysis of the control, *Cdk*13 KD and *Cdk*13 KD + GIVI
1068 groups. A number of differentially expressed genes (DEGs) related to craniofacial development
1069 are shown.
1070
1071

Supplementary Fig. 10

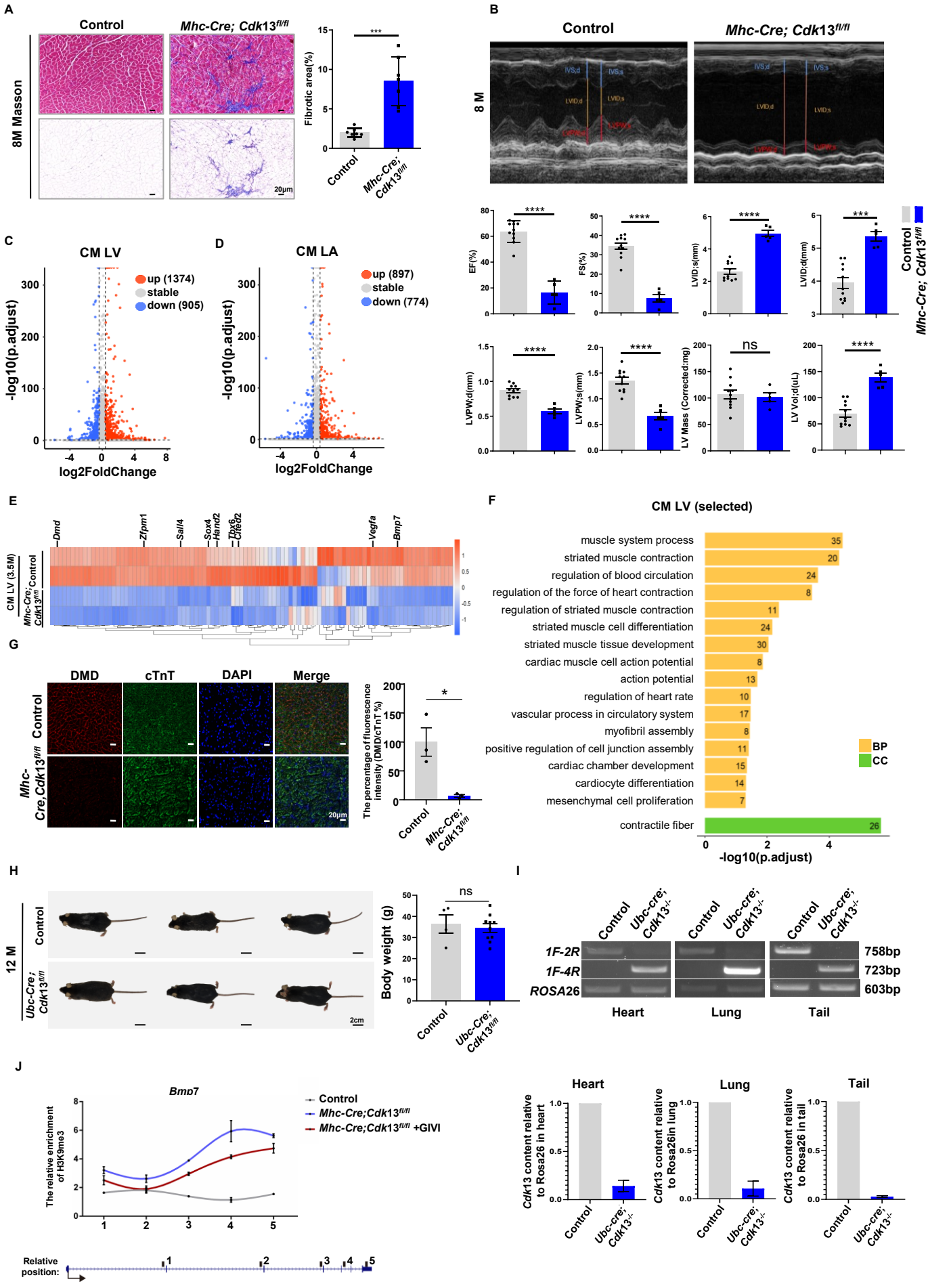

1072 **Supplementary Fig. 10 | Phenotypic and transcriptional analysis of cardiomyocyte-specific**
1073 **deletion of *Cdk*13 in mice and *Cdk*13 deletion-induced H3K9me3 changes in prenatal**
1074 **mouse hearts.**
1075 **A**, Fibrosis significantly accumulated in the hearts of *Mhc-cre;Cdk*13$^{fl/fl}$ mice. The left panel
1076 shows the heart layers of 8-month-old control and *Mhc-Cre;Cdk*13$^{fl/fl}$ mice using Masson's
1077 staining to indicate the pathological fibrosis process. The right panel shows the quantification
1078 analysis of cardiac fibrosis area. The fibrosis area (blue) in the heart tissue was assessed in
1079 Photoshop, and the area was calculated and then divided by the total area to obtain the fibrosis
1080 area; t-test, ***$P < 0.001$, $n = 7$. **B**, Echocardiographic images showed the functional defects by
1081 *Cdk*13 deletion in heart. Eleven control and five knockout mice were analysed. IVS,
1082 interventricular septum; LVID, left ventricular internal diameter; LVPW, left ventricular
1083 posterior wall. EF, ejection fraction; FS, fractional shortening; LVPW;s, left ventricular posterior
1084 wall, systolic; LVPW;d, left ventricular posterior wall, diastolic. T-test, **N**=11(Control)/5(*Mhc-*
1085 *Cre*; *Cdk*13$^{fl/fl}$**)**, ns, not significant; ***$P < 0.001$; ****$P < 0.0001$, t-test. **C, D**, Volcano plot of
1086 DEGs (fold change >1.3 and adjusted $P < 0.1$) in the left ventricle (LV) and left atrium (LA) of
1087 3.5-month-old mice. CM: cardiac muscle. Red points indicate upregulated genes, blue points
1088 indicate downregulated genes, and the dotted line represents the threshold of the fold change and
1089 adjusted P value. **E**, Heatmap of the downregulated genes related to selected Gene Ontology
1090 terms, with a list of genes essential for heart development displayed above. **F**, Selected terms
1091 from Gene Ontology enrichment analysis of downregulated genes in *Cdk*13 mutant. Yellow
1092 represents biological process (BP); green represents cellular component (CC). The x-axis
1093 represents the –log10 (adjusted P value) value, and the numbers on the bars indicate the numbers
1094 of genes enriched for each term. **G**, Cardiomyocyte-specific deletion of *Cdk*13 resulted in a
1095 significant decrease in dystrophic protein (Dmd) expression. The left panel shows fluorescence
1096 staining results using antibodies against Dmd (red) or cTnT (green) of control or *Mhc-*
1097 *Cre;Cdk*13$^{fl/fl}$ hearts of 7-month-old mice. The right panel shows the quantification of the relative
1098 intensity of Dmd. The data are presented as means ± SEMs. *$P < 0.05$, t-test. n=3. **H**, The left
1099 panel represents the body panorama of Control or Ubc-Cre; *Cdk*13$^{fl/fl}$, the right panel shows
1100 statics of body weight(g) in Control or *Ubc-creERT2*; *Cdk*13$^{fl/fl}$ 12-month-old mice. The data are
1101 presented as means ± SEMs. *$P < 0.05$, t-test. **I**, *Cdk*13 deletion efficiency verification. The top
1102 panel shows the PCR verification results of *Cdk*13 deletion efficiency in *Ubc-creERT2*; *Cdk*13$^{fl/fl}$
1103 mice heart(right), lung(middle), and tail(left). The lower panel shows the quantification of the
1104 758bp PCR products. *Rosa*26 was used as the internal control. J. ChIP-qPCR analysis showed
1105 that the enrichment of H3K9me3 in *Cdk*13 knockout embryos was decreased in the presence of
1106 GIVI. The primers were designed to amplify the defined regions in the *Bmp*7.
1107
1108

	Catelog	Name	Molecular weight	Cas number	concentration
1	S1095	Dacinostat（LBH589)	379.459	404951-53-7	0. 2uM
2	S1422	Droxinostat(LAQ824)	243.69	99873-43-5	10uM
3	S2012	PCI-34051	296.32	950762-95-5	5uM
4	S2818	Tacedinaline(CI994)	269.3	112522-64-2	5uM
5	S7229	RGFP966	362.4	1396841-57-8	2uM
6	S7473	Nexturastat A	341.4	1403783-31-2	10uM
7	S8001	Ricolinostat(ACY-1215)	433.5	1316214-52-4	2uM
8	S8043	Scriptaid	326.35	287383-59-9	5uM
9	S2170	Givinostat (ITF2357) Givi	475.97	732302-99-7	2.5nM
10	S7237	OG-L002	225.29	1357302-64-7	2uM
11	S7574	GSK-LSD1 2HCl	289.24	1431368-48-7	2uM
12	S7680	SP2509	437.9	1423715-09-6	2uM
13	S7796	GSK2879552 2HCl	437.4	1401966-69-5 (free pase)	2uM
14	S7572	A-366	329.44	1527503-11-2	1uM
15	S7591	BRD4770	413.47	1374601-40-7	10uM

Supplementary Table 3 | Specific information and working concentrations of 15 small molecule inhibitors used for screening.

Stage	*Cdk*13$^{+/+}$embryos (expected 25%)	*Cdk*13$^{+/-}$embryos (expected 50%)	*Cdk*13$^{-/-}$embryos (expected 25%)	Empty yolk sac/dead	Total number of embryos
E9.5	23 (20.91%)	54 (49.09%)	21 (19.09%)	12 (10.91%)	110
E10.5	48 (30.97%)	58 (37.42%)	37 (23.87%)	12 (7.74%)	155
E11.5	15 (23.08%)	29 (44.62%)	11 (16.92%)	10 (15.38%)	65
E13.5	75 (26.04%)	143 (49.65%)	14 (4.86%)	56 (19.44%)	288
E15.5	8 (20.00%)	22 (55.00%)	0 (0.00%)	10 (25.00%)	40

Supplementary Table. 1 | The genotype and number of surviving *Cdk*13$^{-/-}$ embryos at different stages.

Number	Genotype	Phenotype of E13.5 *Cdk*13$^{-/-}$ embryos
#28-5	*Cdk*13$^{-/-}$	Craniofacial defects, digital anomalies (front left), pleural effusion, back effusion
#28-6	*Cdk*13$^{-/-}$	Craniofacial defects, digital anomalies (front right), pleural effusion, back effusion
#72-1	*Cdk*13$^{-/-}$	Craniofacial defects, digital anomalies (front right), pleural effusion, back effusion
#107-1	*Cdk*13$^{-/-}$	Smaller size, Craniofacial defects, digital anomalies (front right), pleural effusion, back effusion
#135-1	*Cdk*13$^{-/-}$	Smaller size, craniofacial defects, digital anomalies (front left), pleural effusion, back effusion
#141-1	*Cdk*13$^{-/-}$	Craniofacial defects, digital anomalies, pleural effusion, defective neural tube
#433-8	*Cdk*13$^{-/-}$	Smaller size, digital anomalies (front right), pleural effusion
#473-1	*Cdk*13$^{-/-}$	Smaller size, craniofacial defects, digital anomalies (front right), pleural effusion, back effusion
#488-1	*Cdk*13$^{-/-}$	Smaller size, craniofacial defects, digital anomalies (front right), pleural effusion, back effusion
#598-5	*Cdk*13$^{-/-}$	Smaller size, pleural effusion, back effusion.
#748-6	*Cdk*13$^{-/-}$	Smaller size, craniofacial defects, pleural effusion, back effusion, digital anomalies (front left)
#749-8	*Cdk*13$^{-/-}$	Smaller size, craniofacial defects, pleural effusion, back effusion, digital anomalies (front left and front right)
#20-1	*Cdk*13$^{-/-}$	No obvious defects
#598-1	*Cdk*13$^{-/-}$	No obvious defects
#26-4	*Cdk*13$^{-/-}$	Prenatal lethality, craniofacial defects

1114
1115 **Supplementary Table. 2 |** Phenotype of E13.5 Cdk13$^{-/-}$ embryos.
1116
1117